

Hi Frank

Thanks for the comments they were helpful in improving the manuscript.

Please see my response to the comments below. When looking for the line number used in the manuscript please refer to the non-marked up version.

Comment 1:

The first part of section 5.2 and Fig 11 heavily rely on data collected the framework of various aircraft campaigns. I would suggest to include campaign-specific citations here, e.g. for IMECC

Messerschmidt, et al.: Calibration of TCCON column-averaged CO<sub>2</sub>: the first aircraft campaign over European TCCON sites, *Atmospheric Chemistry and Physics*, 11(21), 10765-10777, doi:10.5194/acp-11-10765-2011.

Since we have included citations for the TCCON data sets we acknowledge we should include citations for the aircraft campaigns.

To address this, we have added the following citations on line 306:

Deutscher et al., 2010; Lin et al., 2006; Messerschmidt et al., 2010; Singh et al., 2006; Wofsy, 2011

Comment 2:

Figure 7 included upon request of referee 2 is by far not as informative as it could be. Would you please replace it by separate panels showing XAIR as fct of SZA for the complete datasets, using old and the new linelists? This would demonstrate in a very convincing manner that XAIR is improved (flatter) with the new linelist. Ideally, show separate panels (adding some vertical offset between old and new results for clarity if needed) for each site to reveal any systematic differences between sites (which ideally should not exist).

We have changed Figure 7 to show XAIR plotted as a function of SZA for the entire data set.

The text on lines 244-254 was changed to the following:

"Figure 7 shows XAIR for the entire data set plotted as a function of SZA. XAIR is the column of air (determined using surface pressure recorded at the site) divided by the column of O<sub>2</sub> retrieved from the spectra and multiplied by 0.2095, which is the dry air mole fraction of O<sub>2</sub> in Earth's atmosphere. Ideally XAIR should be 1 but when using O<sub>2</sub> retrieved with a Voigt line shape (Figure 7a) to calculate XAIR the average XAIR value for the entire data set is 0.977. Using O<sub>2</sub> retrieved with the qSDV, to calculate XAIR, the average value is 0.986 which is closer to the expected value of 1. However, XAIR has a dependence on SZA regardless of line shape used. Figure 7a shows that XAIR decreases as a function of SZA (evident at SZA > 75°) which means that the retrieved column of O<sub>2</sub> increases as a function of SZA. Figure 7b shows that XAIR increases as a function of SZA (evident at SZA > 70°), which means that the retrieved column of O<sub>2</sub> decreases as a function of SZA. Therefore retrieving total columns of O<sub>2</sub> with the qSDV changes the airmass dependence of the O<sub>2</sub> column which in turn will impact the airmass dependence of XCO<sub>2</sub>."

The purpose of Figure 7 is to show that (1) XAIR is now closer to the expected value of 1 which is an improvement in the retrieval and (2) that regardless of line shape used the retrieved total column of O<sub>2</sub> has an airmass dependence regardless of spectral. Using the qSDV does not make XAIR (or rather the retrieved total column of O<sub>2</sub>) flatter but rather changes the airmass dependence of O<sub>2</sub>. In section 5.1, we investigate how O<sub>2</sub> retrieved with the qSDV impacts the airmass dependence of XCO<sub>2</sub> which is

shown that it decreases it. Since the total column of CO<sub>2</sub> has an airmass dependence (regardless of spectral line shape used to retrieve it) retrieving a total column of O<sub>2</sub> that was flat as a function of SZA would lead to XCO<sub>2</sub> that would still have an airmass dependence because the total column of CO<sub>2</sub> has an airmass dependence. Figure 8 is showing that the airmass dependence of O<sub>2</sub> retrieved with the qSDV is similar to the airmass dependence of CO<sub>2</sub> so when calculating XCO<sub>2</sub> the airmass dependence of both the CO<sub>2</sub> and O<sub>2</sub> columns almost cancels each other out.

The following text was added on lines 392-397 in the discussion and conclusions section to state that XAIR is now closer to 1 but and airmass dependence of the retrieved O<sub>2</sub> column still remains:

“XAIR calculated with the column of O<sub>2</sub> retrieved with the qSDV is now closer to the expected value of 1 but XAIR still has an airmass dependence which result of the retrieved total column of O<sub>2</sub> decreasing as a function of SZA at large SZA. This remaining airmass dependence could be due to neglecting affects such as Dicke narrowing and line mixing in the absorption coefficient calculations, as well as assuming a perfect instrument line shape in the retrieval algorithm. However, retrieving O<sub>2</sub> with the qSDV significantly decreases the airmass dependence of XCO<sub>2</sub>.”

Comment 3:

Do you think that the retrieved values for the speed dependent shift parameters are significant? The reported error bars are large for at least a subset of lines. Do you recommend for atmospheric work to use the value as reported, or to apply a smooth interpolation in m or to omit the parameters for all lines? Perhaps you could add a short comment on this point in the paper (or I overlooked...)?

To address this comment, we have added the following on line 359-369:

“The large error bars for the measured pressure shifts and speed-dependent pressure shifts as well as a deviation from a smooth m dependence of these parameters could be due to neglecting line mixing when fitting the lab spectra. Figure 3c and 3d show that the spectral lines that have large error bars and deviate from an expected m dependence belong mainly to the Q-branch spectral lines (which are mostly likely impacted by line mixing). To achieve the results obtained in this study it is best to use the parameters as is instead of trying to apply an interpolation, that depends on m, or even omitting them unless one test’s these changes on atmospheric spectra that cover different range of conditions (i.e. seasons, dry/wet, SZA, geographical locations). It is evident that the parameters might be compensating for affects (such as line mixing) that were not included when fitting the lab spectra and changing these parameters (or omitting them) could lead to degradation in the quality of the spectral fits of solar spectra and change the airmass dependence of the retrieved column of O<sub>2</sub> which would impact the airmass dependence of XCO<sub>2</sub>.”

The conclusion "measurements made at SZA > 82 deg no longer have to be discarded" is a bit vague. Do you feel that the SZA range for TCCON should be extended to a new, higher limit (e.g. 86 deg), as supported by datasets from several sites (Fig. 10), or even accept the whole range of SZAs (then only Lamont data - becoming increasingly noisy - remain as supporting evidence)?

Comment 4:

To address this comment, we have added the following on line 398:

“We recommend using the full range of SZA which would result in more XCO<sub>2</sub> measurement available from all TCCON sites.”

Comment 5:

There are a few typos in the new manuscript:

line 12: spectrometers that are part of  
line 32: below  
line 140: are two blanks before "Abrarov"?  
line 214:red line in my printout after "2014a)"  
line 338: missing blank before "(Hartmann"

These typos as well as other formatting issues have been fixed.

Thanks,

Joseph

# 1 Using a Speed-Dependent Voigt Line Shape to Retrieve O<sub>2</sub> from 2 Total Carbon Column Observing Network Solar Spectra to Improve 3 Measurements of XCO<sub>2</sub>

4 Authors: Joseph Mendonca<sup>1</sup>, Kimberly Strong<sup>1</sup>, Debra Wunch<sup>1</sup>, Geoffrey C. Toon<sup>2</sup>, David A.  
5 Long<sup>3</sup>, Joseph T. Hodges<sup>3</sup>, Vincent T. Sironneau<sup>3</sup>, and Jonathan E. Franklin<sup>4</sup>.

6 1. Department of Physics, University of Toronto, Toronto, ON, Canada

7 2. Jet Propulsion Laboratory, Pasadena, CA, USA

8 3. National Institute of Standards and Technology, Gaithersburg, MD, USA

9 4. Harvard John A. Paulson School of Engineering and Applied Sciences, Cambridge, MA, USA

10 *Correspondence to:* Joseph Mendonca ([joseph.mendonca@utoronto.ca](mailto:joseph.mendonca@utoronto.ca))

11 **Abstract.** High-resolution, laboratory, absorption spectra of the  $a^1\Delta_g \leftarrow X^3\Sigma_g^-$  oxygen (O<sub>2</sub>) band measured using  
12 cavity ring-down spectroscopy were fitted using the Voigt and speed-dependent Voigt line shapes. We found that  
13 the speed-dependent Voigt line shape was better able to model the measured absorption coefficients than the Voigt  
14 line shape. We used these line shape models to calculate absorption coefficients to retrieve atmospheric total  
15 columns abundances of O<sub>2</sub> from ground-based spectra from four Fourier transform spectrometers that are part of  
16 the Total Carbon Column Observing Network (TCCON) Lower O<sub>2</sub> total columns were retrieved with the speed-  
17 dependent Voigt line shape, and the difference between the total columns retrieved using the Voigt and speed-  
18 dependent Voigt line shapes increased as a function of solar zenith angle. Previous work has shown that carbon  
19 dioxide (CO<sub>2</sub>) total columns are better retrieved using a speed-dependent Voigt line shape with line mixing. The  
20 column-averaged dry-air mole fraction of CO<sub>2</sub> (XCO<sub>2</sub>) was calculated using the ratio between the columns of CO<sub>2</sub>  
21 and O<sub>2</sub> retrieved (from the same spectra) with both line shapes from measurements made over a one-year period at  
22 the four sites. The inclusion of speed dependence in the O<sub>2</sub> retrievals significantly reduces the airmass dependence  
23 of XCO<sub>2</sub> and the bias between the TCCON measurements and calibrated integrated aircraft profile measurements  
24 was reduced from 1% to 0.4%. These results suggest that speed dependence should be included in the forward  
25 model when fitting near-infrared CO<sub>2</sub> and O<sub>2</sub> spectra to improve the accuracy of XCO<sub>2</sub> measurements.

## 26 1. Introduction

27 Accurate remote sensing of greenhouse gases (GHGs), such as CO<sub>2</sub>, in Earth's atmosphere is important for studying  
28 the carbon cycle to better understand and predict climate change. The absorption of solar radiation by O<sub>2</sub> in the  
29 Earth's atmosphere is important because it can be used to study the properties of clouds and aerosols, and to  
30 determine vertical profiles of temperature and surface pressure. Wallace and Livingston (1990) were the first to  
31 retrieve total columns of O<sub>2</sub> from some of the discrete lines of the  $a^1\Delta_g \leftarrow X^3\Sigma_g^-$  band of O<sub>2</sub> centered at 1.27 μm  
32 (which will be referred to below as the 1.27 μm band) using atmospheric solar absorption spectra from the Kitt

33 Peak observatory. Mlawer et al. (1998) recorded solar absorption spectra in the near-infrared (NIR) region to study  
34 collision-induced absorption (CIA) in the  $a^1\Delta_g \leftarrow X^3\Sigma_g^-$  band as well as two other O<sub>2</sub> bands. The spectra were  
35 compared to a line-by-line radiative transfer model and the differences between the measured and calculated spectra  
36 showed the need for better absorption coefficients in order to accurately model the 1.27 μm band (Mlawer et al.,  
37 1998). Subsequently, spectroscopic parameters needed to calculate the absorption coefficients from discrete  
38 transitions of the 1.27 μm band were measured in multiple studies (Cheah et al., 2000; Newman et al., 1999, 2000;  
39 Smith and Newnham, 2000), as was collision-induced absorption (CIA) (Maté et al., 1999; Smith and Newnham,  
40 2000), while Smith et al. (2001) validated the work done in Smith and Newnham (2000) using solar absorption  
41 spectra.

42 The 1.27 μm band is of particular importance to the Total Carbon Column Observing Network (TCCON) (Wunch  
43 et al., 2011). TCCON is a ground-based remote sensing network that makes accurate and precise measurements of  
44 GHGs for satellite validation and carbon cycle studies. Using the O<sub>2</sub> column retrieved from solar absorption spectra,  
45 the column-averaged dry-air mole fraction of CO<sub>2</sub> (XCO<sub>2</sub>) has been shown to provide better precision than using the  
46 surface pressure to calculate XCO<sub>2</sub> (Yang et al., 2002). The O<sub>2</sub> column is retrieved from the 1.27 μm band because  
47 of its close proximity to the spectral lines used to retrieve CO<sub>2</sub>, thereby reducing the impact of solar tracker mis-  
48 pointing and an imperfect instrument line shape (ILS) (Washenfelder et al., 2006). To improve the retrievals of O<sub>2</sub>  
49 from the 1.27 μm band, Washenfelder et al. (2006) found that adjusting the spectroscopic parameters in HITRAN  
50 2004 (Rothman et al., 2005) decreased the airmass and temperature dependence of the O<sub>2</sub> column. These revised  
51 spectroscopic parameters were included in HITRAN 2008 (Rothman et al., 2009). Atmospheric solar absorption  
52 measurements from this band made at the Park Falls TCCON site by Washenfelder et al. (2006) were the first  
53 measurements to observe the electric-quadrupole transitions (Gordon et al., 2010). Leshchishina et al. (2011, 2010)  
54 subsequently used cavity-ring-down spectra to retrieve spectroscopic parameters for the 1.27 μm band using a Voigt  
55 spectral line shape and these parameters were included in HITRAN 2012 (Rothman et al., 2013). Spectroscopic  
56 parameters for the discrete spectral lines of the O<sub>2</sub> 1.27 μm band from HITRAN 2016 (Gordon et al., 2017) are very  
57 similar to HITRAN 2012 except that HITRAN2016 includes improved line positions reported by Yu et al. (2014).

58 Extensive spectral line shape studies have been performed for the O<sub>2</sub> A-band, which is centered at 762 nm and used  
59 by the Greenhouse Gases Observing Satellite (GOSAT) (Yokota et al., 2009) and the Orbiting Carbon Observatory-  
60 2 (OCO-2) satellite (Crisp et al., 2004) to determine surface pressure. Studies have shown that the Voigt line shape  
61 is inadequate to describe the spectral line shape of the discrete O<sub>2</sub> lines in the A-band. Dicke narrowing occurs when  
62 the motion of the molecule is diffusive due to collisions changing the velocity and direction of the molecule during  
63 the time that it is excited. This diffusive motion is taken into account by averaging over many different Doppler  
64 states resulting in a line width that is narrower than the Doppler width (Dicke, 1953). Long et al. (2010) and Predoi-  
65 Cross et al. (2008) found it necessary to use a spectral Line shape model that accounted for Dicke narrowing when  
66 fitting the discrete lines of the O<sub>2</sub> A-band. Line mixing, which occurs when collisions transfer intensity from one  
67 part of the spectral band to another (Lévy et al., 1992), was shown to be prevalent in multiple studies (Predoi-Cross  
68 et al., 2008; Tran et al., 2006; Tran and Hartmann, 2008). Tran and Hartmann (2008) showed that including line

69 mixing when calculating the O<sub>2</sub> A-band absorption coefficients reduced the airmass dependence of the O<sub>2</sub> column  
 70 retrieved from TCCON spectra. When fitting cavity ring-down spectra of the O<sub>2</sub> A-band, Drouin et al. (2017) found  
 71 it necessary to use a speed-dependence Voigt line shape, which takes into account different speeds at the time of  
 72 collision (Shannon et al., 1986), with line mixing to properly fit the discrete spectral lines of the O<sub>2</sub> A-band.

73 The need to include non-Voigt effects when calculating absorption coefficients for the O<sub>2</sub> 1.27 μm band was first  
 74 shown in Hartmann et al. (2013) and Lamouroux et al. (2014). In Hartmann et al. (2013) and Lamouroux et al.  
 75 (2014), Lorentzian widths were calculated using the re-quantized classical molecular-dynamics simulations  
 76 (rCMDs) and used to fit cavity-ring-down spectra with a Voigt line shape for some isolated transitions in the O<sub>2</sub>  
 77 1.27 μm band. The studies concluded that a Voigt line shape is insufficient for modeling the spectral lines of the O<sub>2</sub>  
 78 1.27 μm band and that effects such as speed dependence and Dicke narrowing should be included in the line shape  
 79 calculation.

80 In this study, air-broadened laboratory cavity-ring-down spectra of the O<sub>2</sub> 1.27 μm band were fitted using a spectral  
 81 line shape that takes into account speed dependence. The derived spectroscopic parameters for the speed-dependent  
 82 Voigt line shape were used to calculate absorption coefficients when fitting high-resolution solar absorption spectra.  
 83 Using these new O<sub>2</sub> total columns, and the simultaneously measured CO<sub>2</sub> total columns, using the updated line  
 84 shape model described by Mendonca et al. (2016), to calculate XCO<sub>2</sub> and compared these results with XCO<sub>2</sub>  
 85 retrieved using a Voigt line shape. Section 2 details the formulas used to calculate absorption coefficients using  
 86 different spectral line shapes. In Section 3, we describe the retrieval of spectroscopic parameters from three air-  
 87 broadened cavity-ring-down spectra fitted with a speed-dependent Voigt line shape. For Section 4, the speed-  
 88 dependent line shape along with the retrieved spectroscopic parameters is used to fit solar absorption spectra from  
 89 four TCCON sites and retrieve total columns of O<sub>2</sub>, which is compared to O<sub>2</sub> retrieved using a Voigt line shape. In  
 90 Section 5, we investigate the change in the airmass dependence of XCO<sub>2</sub> with the new O<sub>2</sub> retrievals. In Section 6, we  
 91 discuss our results and their implications for remote sensing of greenhouse gases.

## 92 **2. Absorption Coefficient Calculations**

### 93 **2.1 Voigt Line Shape**

94 The Voigt line shape is the convolution of the Lorentz and the Gaussian profiles, which model pressure and Doppler  
 95 broadening of the spectral line respectively. The corresponding absorption coefficient,  $k$ , at a given wavenumber  $\nu$   
 96 becomes :

$$k(\nu) = N \sum_j S_j \left( \frac{1}{\gamma_{Dj}} \right) \left( \frac{\ln(2)}{\pi} \right)^{1/2} \left( \text{Re}[c(\nu, x_j, y_j)] \right) \quad (1)$$

97 where  $N$  is the number density,  $S_j$  is the line intensity of spectral line  $j$ ,  $\gamma_{Dj}$  is the Doppler half-width (HWHM),  $c$  is  
 98 the complex error function, and

$$x_j = \frac{(v-v_j^o - P\delta_j^o)}{\gamma_{Dj}} (\ln(2))^{1/2}, \quad y_j = \frac{\gamma_{Lj}}{\gamma_{Dj}} (\ln(2))^{1/2}. \quad (2)$$

99 Here,  $v_j^o$  is the position of the spectral line  $j$ ,  $P$  is the pressure, and  $\delta_j^o$  is the pressure-shift coefficient. The Lorentz  
100 half-width,  $\gamma_{Lj}$ , is calculated using:

$$\gamma_{Lj}(T) = P \gamma_{Lj}^o \left( \frac{296}{T} \right)^n \quad (3)$$

101 where  $\gamma_{Lj}^o$  is the air-broadened Lorentz half-width coefficient (at reference temperature 296 K) and  $n$  is the exponent  
102 of temperature dependence. The Voigt line shape assumes that pressure broadening is accurately represented by a  
103 Lorentz profile calculated for the stastical average velocity at the time of collision.

## 104 2.2 Speed-Dependent Voigt Line Shape

105 The speed-dependent Voigt line shape refines the pressure broadening component of the Voigt by calculating  
106 multiple Lorentz profiles for different speeds at the time of collision. The final contribution from pressure  
107 broadening to the speed-dependent Voigt is the weighted sum of Lorentz profiles (weighted by the Maxwell-  
108 Boltzmann speed-distribution) calculated for different speeds at the time of collision. The speed-dependent Voigt  
109 line shape (Ciuryło, 1998) with the quadratic representation of the Lorentz width and pressure shift (Rohart et al.,  
110 1994) is:

$$k(v) = N \left( \frac{2}{\pi^{3/2}} \right) \sum_j S_j \int_{-\infty}^{\infty} e^{-v^2 V} \left( \tan^{-1} \left[ \frac{x_j - B a_{\delta_j} (V^2 - 1.5) + V}{y_j (1 + a_{\gamma_{Lj}} (V^2 - 1.5))} \right] \right) dV \quad (4)$$

111 where  $a_{\gamma_{Lj}}$  is the speed-dependent Lorentz width parameter (unitless) for line  $j$ ,  $a_{\delta_j}$  is the speed- dependent pressure-  
112 shift parameter (unitless),  $B$  is  $\frac{(\ln(2))^{1/2}}{\gamma_{Dj}}$ ,  $V$  is the ratio of the absorbing molecule's speed to the most probable speed  
113 of the absorbing molecule, and all other variables are defined before.

## 114 3. Fitting Laboratory Spectra

115 O<sub>2</sub>, unlike CO<sub>2</sub> and CH<sub>4</sub>, cannot produce an electric dipole moment and therefore should not be infrared active.  
116 However, O<sub>2</sub> has two unpaired electrons in the ground state that produce a magnetic dipole moment. Due to the  
117 unpaired electrons in the ground state ( $X^3\Sigma_g^-$ ) the rotational state ( $N$ ) is split into three components which are given  
118 by  $J = N-1$ ,  $J = N$ , and  $J = N+1$ , while in the upper state ( $a^1\Delta_g$ ),  $J = N$ . When labeling a transition, the following  
119 nomenclature is used  $\Delta N(N'')\Delta J(J'')$  (Leshchishina et al., 2010), where  $\Delta N$  is the difference between  $N'$  in the upper  
120 state and  $N''$  in the lower state,  $\Delta J$  is the difference between  $J'$  in the upper state and  $J''$  in the lower state. The  
121 magnetic transitions of  $a^1\Delta_g \leftarrow X^3\Sigma_g^-$  allow for  $\Delta J=0, \pm 1$ . This leads to 9 branches observed: P( $N''$ )Q( $J''$ ),  
122 R( $N''$ )Q( $J''$ ), and Q( $N''$ )Q( $J''$ ), for  $\Delta J=0$ , O( $N''$ )P( $J''$ ), P( $N''$ )P( $J''$ ), and Q( $N''$ )P( $J''$ ), for  $\Delta J=-1$ , and S( $N''$ )R( $J''$ ),  
123 R( $N''$ )R( $J''$ ), and Q( $N''$ )R( $J''$ ), for  $\Delta J=1$ .

124 Absorption coefficients for three room temperature air-broadened (NIST Standard reference material® 2659a  
125 containing 79.28 % N<sub>2</sub>, 20.720(43) % O<sub>2</sub>, 0.0029 % Ar, 0.00015 % H<sub>2</sub>O, and 0.001 % other compounds) spectra  
126 were measured at the National Institute of Standards and Technology (NIST) using the frequency-stabilized cavity-  
127 ring-down spectroscopy (FS-CRDS) ) technique (Hodges et al., 2004; Hodges, 2005). The absorption spectra were  
128 acquired at pressures of 131 kPa, 99.3 kPa, and 66.9 kPa, at temperatures of 296.28 K, 296.34 K, and 296.30 K  
129 respectively. Figure 1a shows the three measured absorption spectra. A more detailed discussion of the present FS-  
130 CRDS spectrometer can be found in Lin et al. (2015).

131 The spectra were fitted individually using a Voigt line shape (Eq. 1), with  $S_j$ ,  $\gamma_{L_j}^o$ , and  $\delta_j^o$  for the main isotope of the  
132 magnetic dipole lines of the O<sub>2</sub> 1.27  $\mu\text{m}$  band for lines with an intensity greater than  $7.0 \times 10^{-28} \text{ cm}^{-1}/(\text{molecule cm}^{-2})$ .  
133 The spectroscopic parameters measured in Leshchishina et al. (2011) for the spectral lines of interest were used as  
134 the a priori for the retrieved spectroscopic parameters. The line positions were left fixed to the values measured in  
135 Leshchishina et al. (2011), and all other O<sub>2</sub> spectral lines (intensity less  $7.0 \times 10^{-28} \text{ cm}^{-1}/(\text{molecule cm}^{-2})$ ) were  
136 calculated using a Voigt line shape with spectroscopic parameters from HITRAN 2012 (Rothman et al., 2013).  
137 Spectral fits were done using the lsqnonlin function in Matlab, with a user-defined Jacobian matrix. The Jacobian  
138 was constructed by taking the derivative of the absorption coefficients with respect to the parameters of interest.  
139 Using an analytical Jacobian instead of the finite difference method is both computationally faster and more  
140 accurate. The Voigt line shape was calculated using the Matlab code created by Abrarov and Quine (2011) to  
141 calculate the complex error function and its derivatives. To take collision-induced absorption (CIA) into account, a  
142 set of 50 Legendre polynomials were added together by retrieving the weighting coefficients needed to add the  
143 polynomials to fit the CIA for each spectrum. Figure 1b shows the residual (measured minus calculated absorption  
144 coefficients) when using a Voigt line shape with the retrieved spectroscopic parameters. The plot shows that residual  
145 structure still remains for all three spectra. The Root Mean Square (RMS) residual values for the spectra are given  
146 by the legend at the side of the plot.

147 Figure 2 is the same plot as Figure 1 but for the P(11)P(11), P(11)Q(10), P(9)P(9), and P(9)Q(8) spectral lines only.  
148 Figure 2b shows that for all four spectral lines there is a “W” shaped residual at the line center. The P(11)P(11) line  
149 was also measured by Hartmann et al. (2013) at pressures ranging from 6.7 to 107 kPa. Figure 5 of Hartmann et al.  
150 (2013) shows the P(11)P(11) line at a pressure of 66.7 kPa, which is approximately the pressure of the 66.9 kPa  
151 spectrum (blue spectrum in Figure 1 and 2). When one compares the blue residual of the P(11)P(11) line in Figure  
152 2b to that of the residual of the left panel of Figure 5 of Hartmann et al. (2013), one can see that the residuals are the  
153 same. Figure 6 of Hartmann et al. (2013) show that the amplitude of the residual increases with decreasing pressure,  
154 which is also seen in Figure 2b. Figure 3 of Lamouroux et al. (2014) shows the same “W” residual for the P(9)P(9)  
155 lines and that the amplitude of the residual increases with decreasing pressure (although for lower pressures)  
156 consistent with the results for the P(9)P(9) line in Figure 2b.

157 Figure 1c shows the residual when using the speed-dependent Voigt (Eq. 4) to fit each spectrum individually. To use  
158 Eq. (4) requires integration over all possible speeds, which is not computationally practical, so we employ the

159 simple numerical integration scheme as was done by Wehr (2005). When fitting the spectra, parameters  $S_j$ ,  $\gamma_{L_j}^o$ ,  $\delta_j^o$ ,  
160  $a_{\gamma_{L_i}}$  and  $a_{\delta_j}$  were retrieved for lines of intensity greater than  $7.0 \times 10^{-28} \text{ cm}^{-1}/(\text{molecule cm}^{-2})$ , while all other  $\text{O}_2$  lines  
161 were calculated using a Voigt line shape and spectroscopic parameters from HITRAN 2012 (Rothman et al., 2013b).  
162 The Jacobian matrix was created by taking the derivative with respect to each parameter of interest, as was done  
163 with the Voigt fits. By taking speed-dependent effects into account, the residuals were reduced to 25 times smaller  
164 than those for the Voigt fit and the RMS residuals (given in the legend of Figure 1c) are 10 times smaller. However,  
165 some residual structure still remains, which is more evident in the in the Q and R branches than the P branch. Figure  
166 2c shows the four lines in the P branch, as discussed when analyzing the Voigt fits. A small residual “W” remains at  
167 line center, as well as residuals from weak  $\text{O}_2$  lines.

168 Figure 3 shows the averaged intensity, Lorentz width coefficient, pressure shift coefficient, and speed-dependent  
169 shift coefficient of the  $1.27 \mu\text{m}$   $\text{O}_2$  band, retrieved from the three spectra, plotted as a function of quantum number  
170  $m$  which is  $m=-J$  (where  $J$  is the lower state rotational quantum number) for the P-branch lines,  $m=J$  for the Q-  
171 branch lines, and  $m=J+1$  for the R-branch lines. The intensity, Lorentz widths, and pressure shifts show a  $m$   
172 dependence for these parameters for the P and R sub-branches. The measured Lorentz widths and pressure shifts for  
173 the Q sub-branches show a  $m$  dependence but are not as strong as the P and R sub-branches. This is because the Q  
174 branch lines are broadened enough to blend with each other since they are spaced closer together than the P or R  
175 branch lines. Figure 1c shows that some of the residual structure in the Q branch increases with pressure and is  
176 partly due to the blending of these transitions as the pressure increases. The weak  $\text{O}_2$  absorption lines also blend in  
177 with the Q branch, contributing to the residual structure in Figure 1c. We tried retrieving the spectroscopic  
178 parameters for the weak  $\text{O}_2$  absorption lines, but since they were overlapping with the strong  $\text{O}_2$  lines, it was not  
179 possible. Figure 4a shows the retrieved speed-dependent width parameter averaged over the three spectra, plotted as  
180 a function of  $m$ , showing that it increases with  $m$ . Error bars correspond to the  $2\sigma$  standard deviation and are large  
181 regardless of sub-branch. Figure 4b shows the retrieved speed-dependent width for the PQ sub-branch for the  
182 different pressures. The speed-dependent width shows the same  $m$  dependence regardless of pressure, but also  
183 increases with decreasing pressure as is the case for sub-branches. It should be noted that the speed-dependent width  
184 parameter should be independent of pressure.

#### 185 **4. Fitting Solar Spectra**

186 High-resolution solar absorption spectra were measured at four TCCON sites using a Bruker IFS 125HR FTIR  
187 spectrometer with a room temperature InGaAs detector at a spectral resolution of  $0.02 \text{ cm}^{-1}$  (45 cm maximum  
188 optical path difference). The raw interferograms recorded by the instrument were processed into spectra using the  
189 I2S software package (Wunch, D. et al., 2015) that corrects solar intensity variations (Keppel-Aleks et al., 2007),  
190 phase errors (Mertz, 1967), and laser sampling errors (Wunch, D. et al., 2015), and then performs a fast Fourier  
191 transform to convert the interferograms into spectra (Bergland, 1969). The GGG software package (Wunch, D. et  
192 al., 2015) is used to retrieve total columns of atmospheric trace gases. GFIT is the main code that contains the  
193 forward model, which calculates a solar absorption spectrum using a line-by-line radiative transfer model and an  
194 iterative non-linear least square fitting algorithm that scales an a priori gas profile to obtain the best fit to the

195 measured spectrum. A priori profiles for GHGs are created by an empirical model in GGG that is based on  
196 measurements from the balloon-borne JPL MkIV Fourier Transform Spectrometer (FTS) (Toon, 1991), the  
197 Atmospheric Chemistry Experiment (ACE) FTS instrument aboard SCISAT (Bernath et al., 2005), and in situ  
198 GLOBALVIEW data (Wunch et al., 2011). Temperature and pressure profiles, as well as H<sub>2</sub>O a priori profiles are  
199 generated from the National Centers for Environmental Prediction (NCEP) data. The calculations are performed for  
200 71 atmospheric layers (0 km to 70 km), so all a priori profiles are generated on a vertical grid of 1 km.

201 In the current GGG software package (Wunch, D. et al., 2015), the forward model of GFIT calculates absorption  
202 coefficients for the discrete lines of the O<sub>2</sub> 1.27 μm band using a Voigt line shape and spectroscopic parameters  
203 from Washenfelder et al. (2006a) and Gordon et al. (2010). To take CIA into account, absorption coefficients are  
204 calculated using a Voigt line shape and spectroscopic parameters from the foreign-collision-induced absorption  
205 (FCIA) and self-collision-induced absorption (SCIA) spectral line lists provided with the GGG software package  
206 (Wunch, D. et al., 2015). Spectroscopic parameters in the FCIA and SCIA line lists were retrieved by Geoff Toon by  
207 fitting the laboratory spectra of Smith and Newnham (2000). This was done by retrieving the integrated absorption  
208 at every 1 cm<sup>-1</sup> of the spectrum and using a Voigt line shape, with fixed Lorentz width and no pressure shift. In  
209 GFIT, a volume scale factor is retrieved for the CIA and discrete lines separately so that the O<sub>2</sub> column is derived  
210 from the discrete lines of the 1.27 μm band only. Airglow is not considered when fitting the 1.27 μm band since the  
211 spectrometer views the sun directly, and airglow is overwhelmed by such a bright source. The continuum level and  
212 tilt of the 100% transmission level is fitted using a weighted combination of the first two Legendre polynomials.  
213 Absorption coefficient for all other trace gases are calculated using a Voigt line shape and spectroscopic parameters  
214 from the atm.101 line list (Toon, G. C., 2014a) and solar lines are fitted using the solar line list (Toon, G. C.,  
215 2014b).

216 Figure 5 shows the spectral fit to a solar absorption spectrum recorded at Eureka on March 27, 2015, at a solar  
217 zenith angle (SZA) of 81.32° (airmass of 6.3). This spectrum is an average of 5 Eureka scans. The TCCON standard  
218 is single scan but 5 scans were averaged to decrease the noise. The measured spectrum (red circles), calculated  
219 spectrum (black circles) and transitions from all gases in the window (colored lines, refer to the legend for different  
220 gases) are shown in Figure 5b. The residual obtained using a Voigt line shape to calculate the discrete lines of the O<sub>2</sub>  
221 1.27 μm band is shown in red in Figure 5a. The blue residual is the result of using a speed-dependent Voigt line  
222 shape with the spectroscopic parameters retrieved from fitting the absorption coefficients in Section 3. To decrease  
223 the amount of time it takes to calculate the absorption coefficients, the quadratic-Speed Dependent Voigt (qSDV)  
224 computational approach of Ngo et al. (2013) and Tran et al. (2013) was used instead of Eq. (4) since it requires the  
225 Voigt calculation only twice, while Eq. (4) requires numerical integration scheme with 33 iterations. The  
226 temperature-dependent parameter of the Lorentz width of the discrete lines of the O<sub>2</sub> 1.27 μm band reported in  
227 HITRAN 2012 was used to take temperature dependence into account for  $\gamma_{L_j}(T)$ . There was only a slight  
228 improvement in the fit residuals with the new absorption coefficients (using the qSDV), as seen in Figure 5a.  
229 Absorption coefficients calculated with the qSDV were used to retrieve total columns of O<sub>2</sub> from solar spectra  
230 recorded over a one year period at TCCON sites in Eureka (eu) (Nunavut, Canada) (Batchelor et al., 2009; Strong et

231 al., 2017), Park Falls (pa) (Wisconsin, U.S.A) (Washenfelder et al., 2006; Wennberg et al., 2017) , Lamont (oc)  
232 (Oklahoma, U.S.A) (Wennberg et al., 2017b), and Darwin (db) (Australia) (Deutscher et al., 2010; Griffith et al.,  
233 2017). In total 131 124 spectra were fitted using the qSDV and the average root mean square (RMS) residual of the  
234 fit only decreased by 0.5 %.

## 235 5. Impact of O<sub>2</sub> Columns on XCO<sub>2</sub> Measurements

236 The O<sub>2</sub> column retrieved from the 1.27 μm band with a Voigt line shape and spectroscopic parameters from the  
237 atm.101 line list (Toon, G. C., 2014a) has an airmass dependence such that the O<sub>2</sub> column retrieved increases as a  
238 function of solar zenith angle (or airmass). Using spectra recorded from Eureka, Park Falls, Lamont, and Darwin  
239 over one-year periods, total columns of O<sub>2</sub> were retrieved using (1) a Voigt spectral line shape with spectroscopic  
240 parameters from the atm.101 line list and (2) the qSDV with the spectroscopic parameters determined in Section 3.  
241 Figure 6 shows the percent difference calculated as the column from the qSDV retrieval minus the column from the  
242 Voigt retrieval, which was then divided by the latter and multiplied by 100, plotted as a function of solar zenith  
243 angle (SZA). At the smallest SZA, the qSDV retrieves 0.75% less O<sub>2</sub> than the Voigt, with the difference increasing  
244 to approximately 1.8% as the SZA approaches 90°. Figure 7 shows XAIR ~~from Park Falls on June 18, 2013 for the~~  
245 ~~entire data set plotted as a function of SZA.~~ XAIR is the column of air (determined using surface pressure recorded at  
246 the site) divided by the column of O<sub>2</sub> retrieved from the spectra and multiplied by 0.2095, which is the dry air mole  
247 fraction of O<sub>2</sub> in Earth's atmosphere. Ideally XAIR should be 1 but when using O<sub>2</sub> retrieved with a Voigt line shape  
248 ~~(red points) (Figure 7a) to calculate XAIR it is closer to 0.98 near noon (small SZA) and lower near the start and end~~  
249 ~~of the day (large SZA) the average XAIR value for the entire data set is 0.977. When u~~ Using O<sub>2</sub> retrieved with the  
250 qSDV, ~~to calculate XAIR the average value is 0.986 which is closer to the expected value of 1 is closer to 0.988 near~~  
251 ~~noon and a bit higher near the start and end of the day.~~ However, XAIR has a dependence on SZA regardless of line  
252 shape used. Figure 7a shows that XAIR decreases as a function of SZA (evident at SZA > 75°) which means that the  
253 ~~retrieved column of O<sub>2</sub> increases as a function of SZA. This means the O<sub>2</sub> column, retrieved with the qSDV,~~  
254 ~~decreases as a function of SZA, while previously the column increased as a function of SZA when the Voigt line~~  
255 ~~shape is used.~~ Figure 7b shows that XAIR increases as a function of SZA (evident at SZA > 70°), which means that  
256 ~~the retrieved column of O<sub>2</sub> now decreases as a function of SZA. Therefore retrieving total columns of O<sub>2</sub> with the~~  
257 ~~qSDV changes the airmass dependence of the O<sub>2</sub> column which in turn will impact the airmass dependence of~~  
258 ~~XCO<sub>2</sub>.~~

### 259 5.1 Airmass Dependence of XCO<sub>2</sub>

260 Since the standard TCCON XCO<sub>2</sub> (and all other XGas) is calculated using the column of O<sub>2</sub> instead of the surface  
261 pressure, errors associated with the retrieval of O<sub>2</sub>, such as the airmass dependence of the O<sub>2</sub> column, will affect  
262 XCO<sub>2</sub>. Figure 8 is XCO<sub>2</sub> calculated for four different combinations pertaining to the two CO<sub>2</sub> column retrievals and  
263 the O<sub>2</sub> column retrievals. The CO<sub>2</sub> columns were retrieved with either a Voigt line shape (the standard GGG2014  
264 approach) or the qSDV with line mixing as done in Mendonca et al. (2016) while the O<sub>2</sub> columns were retrieved  
265 with either a Voigt (the standard GGG2014 approach) or the new qSDV approach developed here. Figure 8 shows a

266 spurious symmetric component to XCO<sub>2</sub> when the total column of O<sub>2</sub> is retrieved with the Voigt line shape,  
 267 regardless of line shape used to retrieve CO<sub>2</sub>. When the qSDV is used to retrieve total columns of O<sub>2</sub>, the symmetric  
 268 component of XCO<sub>2</sub> is dismissed regardless of line shape used to retrieve CO<sub>2</sub>. This is because the airmass  
 269 dependence of the column of O<sub>2</sub> retrieved using the qSDV is more consistent with the airmass dependence of the  
 270 column of CO<sub>2</sub> (for both line shapes used to retrieve CO<sub>2</sub>). Mendonca et al. (2016) showed that using the qSDV with  
 271 line mixing results in better fits to the CO<sub>2</sub> windows and impacts the airmass dependence of the retrieved column of  
 272 CO<sub>2</sub>. When using a Voigt line shape the retrieved column amount of CO<sub>2</sub> decreases as airmass increases until the  
 273 airmass is large (SZA of about 82°) at which point the retrieved column of CO<sub>2</sub> increases as the airmass increases,  
 274 changing the shape of the airmass dependence of the CO<sub>2</sub> column. When the qSDV with line mixing is used, the  
 275 retrieved column of CO<sub>2</sub> decreases as a function of airmass (up until the sun is above the horizon).

276 To correct for this, an empirical correction is applied to all TCCON XCO<sub>2</sub> (and XGas). The empirical correction  
 277 determines the antisymmetrical component of the day's XCO<sub>2</sub>, which is assumed to be the true variation of XCO<sub>2</sub>  
 278 throughout the day, as well as the symmetrical component, which is caused by the airmass dependence of the  
 279 retrieved column of the gas of interest and O<sub>2</sub>. We can, therefore, represent a measurement as (Wunch et al., 2011):

$$y_i = \hat{y}[1 + \alpha S(\theta_i) + \beta A(t_i)] \quad (5)$$

280 where  $\hat{y}$  is the mean value of XCO<sub>2</sub> measured that day,  $\beta$  is the fitted coefficient of the antisymmetric function  $A(t_i)$   
 281 and  $\alpha$  is the fitted coefficient of the symmetric function  $S(\theta_i)$ . The antisymmetric function is calculated by (Wunch  
 282 et al., 2011):

$$A(t_i) = \sin(2\pi(t_i - t_{noon})) \quad (6)$$

283 where  $t_i$  is the time of the measurement and  $t_{noon}$  is the time at solar noon, both in units of days. The symmetric  
 284 function is calculated by (Wunch et al., 2011):

$$S(\theta_i) = \left(\frac{\theta_i + 13^\circ}{90^\circ + 13^\circ}\right)^3 - \left(\frac{45^\circ + 13^\circ}{90^\circ + 13^\circ}\right)^3 \quad (7)$$

285 where  $\theta_i$  is the SZA in degrees. To determine  $\alpha$  for the different line shapes, total columns of CO<sub>2</sub> were retrieved  
 286 using the Voigt line shape (Wunch, D. et al., 2015) and the qSDV with line mixing (Mendonca et al., 2016).  
 287 Henceforth, we will refer to XCO<sub>2</sub> calculated from O<sub>2</sub> and CO<sub>2</sub> using the Voigt line shape as XCO<sub>2</sub> Voigt and the  
 288 qSDV line shape as XCO<sub>2</sub> qSDV.

289 Figure 9 shows the average  $\alpha$  calculated for each season at Darwin, Lamont, and Park Falls. Eureka XCO<sub>2</sub> cannot be  
 290 used to determine  $\alpha$  because Eureka measurements do not go through the same range of SZAs as the other three  
 291 sites due to its geolocation. The average  $\alpha$  values derived from XCO<sub>2</sub> Voigt are represented by stars in Figure 9,  
 292 while the squares indicate XCO<sub>2</sub> qSDV. At all three sites,  $\alpha$  is closer to 0 when the qSDV line shape is used in the  
 293 retrieval compared to the Voigt retrieval, regardless of the season. The average  $\alpha$  for XCO<sub>2</sub> Voigt calculated from a

294 year of measurements from Darwin, Park Falls, and Lamont is  $-0.0071 \pm 0.0057$  and that for XCO<sub>2</sub> qSDV is -  
295  $0.0012 \pm 0.0054$ .

296 For all four sites,  $\alpha = -0.0071$  is used to correct XCO<sub>2</sub> Voigt measurements. Figure 10a shows the XCO<sub>2</sub> Voigt  
297 anomalies plotted as a function of SZA. The data is expressed as the daily XCO<sub>2</sub> anomaly, which is the difference  
298 between the XCO<sub>2</sub> value and the daily median value, in order to remove the seasonal cycle. When XCO<sub>2</sub> is left  
299 uncorrected for airmass dependencies, XCO<sub>2</sub> decreases as a function of SZA up to approximately 82°, and increases  
300 as a function of SZA at angles greater than 82°. Figure 10b shows XCO<sub>2</sub> Voigt corrected for the airmass  
301 dependence. This airmass correction works well only up to a SZA of approximately 82°. Figure 10c is the same as  
302 10a but for the uncorrected XCO<sub>2</sub> qSDV measurements, while Figure 10d is the same as 10b but for the corrected  
303 XCO<sub>2</sub> qSDV measurements. When the airmass correction is applied to XCO<sub>2</sub> qSDV there is a small difference  
304 between the corrected and uncorrected XCO<sub>2</sub> qSDV measurements, with the difference only noticeable for the  
305 Darwin measurements recorded at SZA > 60°. For XCO<sub>2</sub> qSDV measurements made at SZA > 82° XCO<sub>2</sub> does not  
306 increase with SZA as it does with the Voigt.

## 307 **5.2 Accuracy of XCO<sub>2</sub>**

308 To assess the accuracy of TCCON XCO<sub>2</sub> measurements, they are compared to aircraft XCO<sub>2</sub> profile measurements  
309 using the method described in Wunch et al. (2010). Figure 11a shows the comparison between the aircraft XCO<sub>2</sub>  
310 (Deutscher et al., 2010; Lin et al., 2006; Messerschmidt et al., 2010; Singh et al., 2006; Wofsy, 2011) measurements  
311 (legend at the top details the different aircraft) and TCCON XCO<sub>2</sub> Voigt measurements for 13 TCCON sites (given  
312 by the color-coded legend at the bottom right). The gray line indicates the one-to-one line and the dashed line is the  
313 line of best fit. There is a bias of  $0.9897 \pm 0.0005$ , as given by the slope of the line of best fit in Figure 11a, for the  
314 XCO<sub>2</sub> Voigt measurements. Figure 11b is the same as 11a but for the XCO<sub>2</sub> qSDV measurements. The bias between  
315 the aircraft XCO<sub>2</sub> measurements and the XCO<sub>2</sub> qSDV measurements is  $1.0041 \pm 0.0005$  as given by the slope of the  
316 line of best fit in Figure 11b. This increase in the slope can be explained by an increase in the retrieved column of  
317 CO<sub>2</sub> when using the qSDV with line mixing as shown in Mendonca et al. (2016) as well as combined with a  
318 decrease in the retrieved O<sub>2</sub> column due to using the qSDV. As discussed previously (section 5) the decrease in the  
319 retrieved O<sub>2</sub> column is an improvement but the expected column of O<sub>2</sub> is still approximately 1.2% higher (at the  
320 smallest SZA) than it should be. Therefore, the retrieved column of CO<sub>2</sub> is higher than it should be, and the slope  
321 would be greater if the retrieved column of O<sub>2</sub> was 1.2% lower. Never the less using the qSDV to retrieve total  
322 columns of CO<sub>2</sub> and O<sub>2</sub> reduces the difference between TCCON XCO<sub>2</sub> and aircraft XCO<sub>2</sub> measurements by 0.62 %.

323 TCCON XCO<sub>2</sub> measurements are divided by the scale factors (or bias determined in Figure 11) to calibrate to the  
324 WMO scale. For all TCCON XCO<sub>2</sub> measurements retrieved with a Voigt line shape, the airmass correction is first  
325 applied to the data and the result is divided by the determined bias factor, 0.9897. Figure 12a to 12d shows XCO<sub>2</sub>  
326 Voigt (for Eureka, Park Falls, Lamont, and Darwin respectively) indicated by red square boxes in the plots. XCO<sub>2</sub>  
327 Voigt measurements made at SZA > 82° have been filtered out because they cannot be corrected for the airmass  
328 dependence. The blue boxes are XCO<sub>2</sub> qSDV corrected for airmass dependence and scaled by 1.0041. No filter was

329 applied to the XCO<sub>2</sub> qSDV measurements for SZA since the airmass dependence correction works at all SZA.  
330 Figure 12e to 12h shows the difference between XCO<sub>2</sub> Voigt and XCO<sub>2</sub> qSDV for Eureka, Park Falls, Lamont, and  
331 Darwin respectively. The mean differences for the data shown in Figures 12e to 12h are 0.113±0.082, -0.102±0.223,  
332 -0.132±0.241, and -0.059±0.231 μmol/mol (ppm) for Eureka, Park Falls, Lamont, and Darwin respectively. The  
333 difference throughout the day at Park Falls, Lamont, and Darwin varies between -0.6 to 0.2 μmol/mol and is SZA  
334 dependent.

335 Figure 13a shows XCO<sub>2</sub> Voigt corrected for the airmass dependence, as well as XCO<sub>2</sub> qSDV, uncorrected and  
336 corrected for the airmass dependence. These XCO<sub>2</sub> measurements were retrieved from Park Falls spectra recorded  
337 on June 18, 2013. For all three XCO<sub>2</sub> measurements, the amount of XCO<sub>2</sub> decreases throughout the day. Figure 13b  
338 shows the difference between the corrected Voigt XCO<sub>2</sub> and the uncorrected qSDV XCO<sub>2</sub>, as well as the difference  
339 between the corrected Voigt XCO<sub>2</sub> and the corrected qSDV XCO<sub>2</sub>. The difference between the Voigt and the qSDV  
340 (corrected and uncorrected) shows that at the start and end of the day, more XCO<sub>2</sub> is retrieved with the qSDV, while  
341 at midday less is retrieved with the qSDV. The range in the differences seen in Figure 12e to 12h varies with SZA  
342 throughout the day as shown in Figure 13b.

## 343 6. Discussion and Conclusions

344 Using cavity ring-down spectra measured in the lab, we have shown that the Voigt line shape is insufficient to  
345 model the line shape of O<sub>2</sub> for the 1.27 μm band, consistent with the results of (Hartmann et al. (2013) and  
346 Lamouroux et al. (2014). By using the speed-dependent Voigt line shape when calculating the absorption  
347 coefficients, we were better able to reproduce the measured absorption coefficients than using the Voigt line shape.  
348 However, some residual structure remains as seen Figures 1 and 2. This is partly due to the blending of spectral lines  
349 (i.e., line mixing) and the inability to retrieve the spectroscopic parameters for weak O<sub>2</sub> transitions. Fitting low-  
350 pressure spectra would help with isolating spectral lines and decreasing the uncertainty on the retrieved  
351 spectroscopic parameters for the Q branch lines.

352 Accurate measurements of the pressure shifts in the 1.27 μm band have been hard to obtain as shown in Newman et  
353 al. (1999) and Hill et al., (2003). While the retrieved pressure shifts show a dependence on quantum number m  
354 (Figure 3c) as one would expect, this dependence is not as strong as the m dependence of the Lorentz widths (Figure  
355 3b). This can be explained by the fact that line mixing, which is shown to be important for the O<sub>2</sub> A-band, was not  
356 considered when fitting the cavity-ringdown spectra. Neglecting line mixing usually produces an asymmetric  
357 residual in the discrete lines as well as a broad residual feature associated with the fact that collisions are transferring  
358 intensity from one part of the spectrum to another. By fitting a set of Legendre polynomials for CIA we could be  
359 simultaneously fitting the broader band feature associated with line mixing while the retrieved pressure shifts, and  
360 speed-dependent pressure shifts could be compensating for the asymmetric structure one would see in the discrete  
361 lines when neglecting line mixing. The remaining structure, as seen in Figure 1c, could be due to neglecting line  
362 mixing especially in the Q-branch where the spacing between spectral lines is small (in comparison to the P and R  
363 branches) and line mixing is most likely prevalent. The large error bars for the measured pressure shifts and speed-

364 dependent pressure shifts as well as a deviation from a smooth  $m$  dependence of these parameters could be due to  
365 neglecting line mixing when fitting the lab spectra. Figure 3c and 3d show that the spectral lines that have large error  
366 bars and deviate from an expected  $m$  dependence belong mainly to the Q-branch spectral lines (which are mostly  
367 likely impacted by line mixing). To achieve the results obtained in this study it is best to use the parameters as is  
368 instead of trying to apply an interpolation, that depends on  $m$ , or even omitting them unless one test's these changes  
369 on atmospheric spectra that cover different range of conditions (i.e seasons, dry/wet, SZA, geographical locations).  
370 It is evident that the parameters might be compensating for affects (such as line mixing) that were not included when  
371 fitting the lab spectra and changing these parameters (or omitting them) could lead to degradation in the quality of  
372 the spectral fits of solar spectra and change the airmass dependence of the retrieved column of  $O_2$  which would  
373 impact the airmass dependence of  $XCO_2$ .

374 The pressure dependence of the retrieved speed-dependent width parameter is an indication that Dicke narrowing  
375 needs to be taken into account, as shown by Bui et al. (2014) for  $CO_2$ . When both speed dependence and Dicke  
376 narrowing are present, a multi-spectrum fit needs to be used due to the correlation between the parameters (Bui et  
377 al., 2014). Domysławska et al. (2016) recommend using the qSDV to model the line shape of  $O_2$  based on multiple  
378 line shape studies of the  $O_2$  B-band. In these studies, a multi-spectrum fit to low pressure (0.27-5.87 kPa) cavity-ring  
379 down spectra was performed testing multiple line shapes that took speed-dependence and Dicke narrowing into  
380 account both separately and simultaneously. They found that the line shapes that only used Dicke narrowing were  
381 not good enough to model the line shape of the  $O_2$  B-band lines, but a line shape that included either speed-  
382 dependence or both speed-dependence and Dicke narrowing produced similar quality fits, ultimately concluding that  
383 speed-dependence has a larger effect than Dicke narrowing. It was noted in the study by Wójtewicz et al., (2014)  
384 that both Dicke narrowing and speed-dependent effects might simultaneously play an important role in modeling the  
385 line shape of the  $O_2$  B-band lines. However, the speed-dependent and Dicke narrowing parameters are highly  
386 correlated at low pressures. To reduce the correlation requires either a multi-spectrum fit of spectra at low pressures  
387 with high enough signal to noise ratio or spectra that cover a wide range of pressure (Wójtewicz et al., 2014). So, by  
388 combining the high-pressure spectra used in this study with low pressure spectra in a multispectrum fit both the  
389 speed-dependence and Dicke narrowing parameters could be retrieved. The temperature dependence of the Lorentz  
390 width coefficients of this band has never been measured before, which could have an impact on the airmass  
391 dependence of  $O_2$ . Combining high-pressure cavity-ring-down absorption coefficient measurements with those for  
392 low pressures and different temperatures as done in Devi et al. (2015 and 2016) for  $CH_4$  would lead to more accurate  
393 line shape parameters for  $O_2$ .

394 By taking speed dependence into account for both  $CO_2$  (in the work of Mendonca et al., 2016) and  $O_2$  (the work  
395 presented here), we were able to significantly decrease the airmass dependence of TCCON  $XCO_2$  and the bias  
396 between TCCON and aircraft  $XCO_2$ .  $XAIR$  calculated with the column of  $O_2$  retrieved with the qSDV is now closer  
397 to the expected value of 1 but  $XAIR$  still has an airmass dependence which is the result of the retrieved total column  
398 of  $O_2$  decreasing as a function of SZA at large SZA. This remaining airmass dependence could be due to neglecting  
399 affects such as Dicke narrowing and line mixing in the absorption coefficient calculations, as well as assuming a

400 perfect instrument line shape in the retrieval algorithm. However, retrieving O<sub>2</sub> with the qSDV significantly  
401 decreases the airmass dependence of XCO<sub>2</sub>. With the qSDV line shape, XCO<sub>2</sub> measurements made at SZA > 82° no  
402 longer have to be discarded. We recommend using the full range of SZA which would result in more XCO<sub>2</sub>  
403 measurement available from all TCCON sites. This is particularly important for high-latitude TCCON sites, such as  
404 Eureka, because measurements made from late February to late March and from late September until mid-October  
405 are made at SZA > 82°. Filtering out these large SZA measurements thus limits the knowledge of the seasonal cycle  
406 of XCO<sub>2</sub> at high latitudes. The airmass dependence of the O<sub>2</sub> column not only effects XCO<sub>2</sub> but all trace gases  
407 measured by TCCON and in the future the airmass dependence of all XGas will be determined with these new O<sub>2</sub>  
408 columns.

#### 409 **Acknowledgements**

410 This work was primarily supported by the Canadian Space Agency (CSA) through the GOSAT and CAFTON  
411 projects and the Natural Sciences and Engineering Research Council of Canada (NSERC). The Eureka  
412 measurements were made at the Polar Environment Atmospheric Research Laboratory (PEARL) by the Canadian  
413 Network for the Detection of Atmospheric Change (CANDAC), which has been supported by the AIF/NSRIT, CFI,  
414 CFCAS, CSA, Environment Canada (EC), Government of Canada IPY funding, NSERC, OIT, ORF, PCSP, and  
415 FQRNT. The authors wish to thank the staff at EC's Eureka Weather Station and CANDAC for the logistical and  
416 on-site support provided. Thanks to CANDAC Principal Investigator James R. Drummond, PEARL Site Manager  
417 Pierre Fogal, and CANDAC/PEARL operators Mike Maurice and Peter McGovern, for their invaluable assistance in  
418 maintaining and operating the Bruker 125HR. The research at the Jet Propulsion Laboratory (JPL), and California  
419 Institute of Technology was performed under contracts and cooperative agreements with the National Aeronautics  
420 and Space Administration (NASA). Geoff Toon and Debra Wunch acknowledge support from NASA for  
421 the development of TCCON via grant number NNX17AE15G. Darwin TCCON measurements are possible thanks  
422 to support from NASA grants NAG5-12247 and NNG05-GD07G, the Australian Research Council grants  
423 DP140101552, DP110103118, DP0879468 and LP0562346, and the DOE ARM program for technical support. The  
424 research at the National Institute of Standards and Technology was performed with the support of the NIST  
425 Greenhouse Gas Measurements and Climate Research Program. Certain commercial equipment, instruments, or  
426 materials are identified in this paper in order to specify the experimental procedure adequately. Such identification is  
427 not intended to imply recommendation or endorsement by the National Institute of Standards and Technology, nor is  
428 it intended to imply that the materials or equipment identified are necessarily the best available for the purpose.

429

430

431

432

433

434 **References**

- 435 Abrarov, S.M., Quine, B.M.: Efficient algorithmic implementation of the Voigt/complex error function based on  
436 exponential series approximation. *Appl. Math. Comput.* 218, 1894–1902.  
437 <https://doi.org/10.1016/j.amc.2011.06.072>, 2011.
- 438 Batchelor, R.L., Strong, K., Lindenmaier, R., Mittermeier, R.L., Fast, H., Drummond, J.R., Fogal, P.F.: A New  
439 Bruker IFS 125HR FTIR Spectrometer for the Polar Environment Atmospheric Research Laboratory at  
440 Eureka, Nunavut, Canada: Measurements and Comparison with the Existing Bomem DA8 Spectrometer. *J.*  
441 *Atmospheric Ocean. Technol.* 26, 1328–1340. <https://doi.org/10.1175/2009JTECHA1215.1>, 2009.
- 442 Bergland, G.: A radix-eight fast Fourier transform subroutine for real-valued series. *IEEE Trans. Audio*  
443 *Electroacoustics* 17, 138–144. <https://doi.org/10.1109/TAU.1969.1162043>, 1969.
- 444 Bernath, P.F., McElroy, C.T., Abrams, M.C., Boone, C.D., Butler, M., Camy-Peyret, C., Carleer, M., Clerbaux, C.,  
445 Coheur, P.-F., Colin, R., DeCola, P., DeMazière, M., Drummond, J.R., Dufour, D., Evans, W.F.J., Fast, H.,  
446 Fussen, D., Gilbert, K., Jennings, D.E., Llewellyn, E.J., Lowe, R.P., Mahieu, E., McConnell, J.C.,  
447 McHugh, M., McLeod, S.D., Michaud, R., Midwinter, C., Nassar, R., Nichitiu, F., Nowlan, C., Rinsland,  
448 C.P., Rochon, Y.J., Rowlands, N., Semeniuk, K., Simon, P., Skelton, R., Sloan, J.J., Soucy, M.-A., Strong,  
449 K., Tremblay, P., Turnbull, D., Walker, K.A., Walkty, I., Wardle, D.A., Wehrle, V., Zander, R., Zou, J.:  
450 Atmospheric Chemistry Experiment (ACE): Mission overview. *Geophys. Res. Lett.* 32, L15S01.  
451 <https://doi.org/10.1029/2005GL022386>, 2005.
- 452 Bui, T.Q., Long, D.A., Cygan, A., Sironneau, V.T., Hogan, D.W., Rupasinghe, P.M., Ciuryło, R., Lisak, D.,  
453 Okumura, M.: Observations of Dicke narrowing and speed dependence in air-broadened CO<sub>2</sub> lineshapes  
454 near 2.06 μm. *J. Chem. Phys.* 141, 174301. <https://doi.org/10.1063/1.4900502>, 2014.
- 455 Cheah, S.-L., Lee, Y.-P., Ogilvie, J.F.: Wavenumbers, strengths, widths and shifts with pressure of lines in four  
456 bands of gaseous 16O<sub>2</sub> in the systems  $a^1\Delta_g-X^3\Sigma_g^-$  and  $b^1\Sigma_g^+-X^3\Sigma_g^-$ . *J. Quant. Spectrosc. Radiat. Transf.*  
457 64, 467–482. [https://doi.org/10.1016/S0022-4073\(99\)00126-0](https://doi.org/10.1016/S0022-4073(99)00126-0), 2000.
- 458 Ciuryło, R.: Shapes of pressure- and Doppler-broadened spectral lines in the core and near wings. *Phys. Rev. A* 58,  
459 1029–1039. <https://doi.org/10.1103/PhysRevA.58.1029>, 1998.
- 460 Crisp, D., Atlas, R.M., Breon, F.-M., Brown, L.R., Burrows, J.P., Ciaï, P., Connor, B.J., Doney, S.C., Fung, I.Y.,  
461 Jacob, D.J., Miller, C.E., O'Brien, D., Pawson, S., Randerson, J.T., Rayner, P., Salawitch, R.J., Sander,  
462 S.P., Sen, B., Stephens, G.L., Tans, P.P., Toon, G.C., Wennberg, P.O., Wofsy, S.C., Yung, Y.L., Kuang, Z.,  
463 Chudasama, B., Sprague, G., Weiss, B., Pollock, R., Kenyon, D., Schroll, S.: The Orbiting Carbon  
464 Observatory (OCO) mission. *Adv. Space Res., Trace Constituents in the Troposphere and Lower*  
465 *Stratosphere* 34, 700–709. <https://doi.org/10.1016/j.asr.2003.08.062>, 2004.
- 466 Deutscher, N.M., Griffith, D.W.T., Bryant, G.W., Wennberg, P.O., Toon, G.C., Washenfelder, R.A., Keppel-Aleks,  
467 G., Wunch, D., Yavin, Y., Allen, N.T., Blavier, J.-F., Jiménez, R., Daube, B.C., Bright, A.V., Matross,  
468 D.M., Wofsy, S.C., Park, S.: Total column CO<sub>2</sub> measurements at Darwin, Australia – site description and  
469 calibration against in situ aircraft profiles. *Atmos Meas Tech* 3, 947–958. [https://doi.org/10.5194/amt-3-](https://doi.org/10.5194/amt-3-947-2010)  
470 947-2010, 2010.
- 471 Devi, V.M., Benner, D.C., Sung, K., Brown, L.R., Crawford, T.J., Yu, S., Smith, M.A.H., Mantz, A.W., Boudon,  
472 V., Ismail, S.: Spectral line parameters including line shapes in the 2ν<sub>3</sub> Q branch of 12CH<sub>4</sub>. *J. Quant.*  
473 *Spectrosc. Radiat. Transf., XVIIIth Symposium on High Resolution Molecular Spectroscopy (HighRus-*  
474 *2015)*, Tomsk, Russia 177, 152–169. <https://doi.org/10.1016/j.jqsrt.2015.12.009>, 2016.
- 475 Devi, V.M., Benner, D.C., Sung, K., Crawford, T.J., Yu, S., Brown, L.R., Smith, M.A.H., Mantz, A.W., Boudon,  
476 V., Ismail, S.: Self- and air-broadened line shapes in the 2ν<sub>3</sub> P and R branches of 12CH<sub>4</sub>. *J. Mol.*  
477 *Spectrosc., Spectroscopy with Synchrotron Radiation* 315, 114–136.  
478 <https://doi.org/10.1016/j.jms.2015.05.003>, 2015.
- 479 Dicke, R.H.: The Effect of Collisions upon the Doppler Width of Spectral Lines. *Phys. Rev.* 89, 472–473.  
480 <https://doi.org/10.1103/PhysRev.89.472>, 1953.
- 481 Domysławska, J., Wójtewicz, S., Masłowski, P., Cygan, A., Bielska, K., Trawiński, R.S., Ciuryło, R., Lisak, D.: A  
482 new approach to spectral line shapes of the weak oxygen transitions for atmospheric applications. *J. Quant.*  
483 *Spectrosc. Radiat. Transf.* 169, 111–121. <https://doi.org/10.1016/j.jqsrt.2015.10.019>, 2016.
- 484 Drouin, B.J., Benner, D.C., Brown, L.R., Cich, M.J., Crawford, T.J., Devi, V.M., Guillaume, A., Hodges, J.T.,  
485 Mlawer, E.J., Robichaud, D.J., Oyafuso, F., Payne, V.H., Sung, K., Wishnow, E.H., Yu, S.: Multispectrum  
486 analysis of the oxygen A-band. *J. Quant. Spectrosc. Radiat. Transf., Satellite Remote Sensing and*  
487 *Spectroscopy: Joint ACE-Odin Meeting, October 2015* 186, 118–138.  
488 <https://doi.org/10.1016/j.jqsrt.2016.03.037>, 2017.

489 Gordon, I.E., Kassı, S., Campargue, A., Toon, G.C.: First identification of the electric quadrupole transitions of  
490 oxygen in solar and laboratory spectra. *J. Quant. Spectrosc. Radiat. Transf.*, Special Issue Dedicated to  
491 Laurence S. Rothman on the Occasion of his 70th Birthday. 111, 1174–1183.  
492 <https://doi.org/10.1016/j.jqsrt.2010.01.008>, 2010.

493 Gordon, I.E., Rothman, L.S., Hill, C., Kochanov, R.V., Tan, Y., Bernath, P.F., Birk, M., Boudon, V., Campargue,  
494 A., Chance, K.V., Drouin, B.J., Flaud, J.-M., Gamache, R.R., Hodges, J.T., Jacquemart, D., Perevalov, V.I.,  
495 Perrin, A., Shine, K.P., Smith, M.-A.H., Tennyson, J., Toon, G.C., Tran, H., Tyuterev, V.G., Barbe, A.,  
496 Császár, A.G., Devi, V.M., Furtenbacher, T., Harrison, J.J., Hartmann, J.-M., Jolly, A., Johnson, T.J.,  
497 Karman, T., Kleiner, I., Kyuberis, A.A., Loos, J., Lyulin, O.M., Massie, S.T., Mikhailenko, S.N., Moazzen-  
498 Ahmadi, N., Müller, H.S.P., Naumenko, O.V., Nikitin, A.V., Polyansky, O.L., Rey, M., Rotger, M.,  
499 Sharpe, S.W., Sung, K., Starikova, E., Tashkun, S.A., Auwera, J.V., Wagner, G., Wilzewski, J., Wcislo, P.,  
500 Yu, S., Zak, E.J.: The HITRAN2016 molecular spectroscopic database. *J. Quant. Spectrosc. Radiat.*  
501 *Transf.*, HITRAN2016 Special Issue 203, 3–69. <https://doi.org/10.1016/j.jqsrt.2017.06.038>, 2017.

502 Griffith, D.W.T., Deutscher, N.M., Velazco, V.A., Wennberg, P.O., Yavin, Y., Keppel-Aleks, G., Washenfelder,  
503 R.A., Toon, G.C., Blavier, J.-F., Paton-Walsh, C., Jones, N.B., Kettlewell, G.C., Connor, B.J., Macatangay,  
504 R.C., Roehl, C., Ryzek, M., Glowacki, J., Culgan, T., Bryant, G.W.: TCCON data from Darwin (AU),  
505 Release GGG2014.R0. <https://doi.org/10.14291/tcon.ggg2014.darwin01.R0/1149290>, 2017.

506 Hartmann, J.-M., Sironneau, V., Boulet, C., Svensson, T., Hodges, J.T., Xu, C.T.: Collisional broadening and  
507 spectral shapes of absorption lines of free and nanopore-confined O<sub>2</sub> gas. *Phys. Rev. A* 87, 032510.  
508 <https://doi.org/10.1103/PhysRevA.87.032510>, 2013.

509 Hill, C., Brown, J.M., Newnham, D.A.: An upper limit for the magnitude of pressure shifts in the O<sub>2</sub>  
510 a<sup>1</sup>Δ<sub>g</sub>←X<sup>3</sup>Σ<sub>g</sub><sup>-</sup>(0–0) band. *J. Mol. Spectrosc.* 221, 286–287. [https://doi.org/10.1016/S0022-2852\(03\)00227-3](https://doi.org/10.1016/S0022-2852(03)00227-3),  
511 2003.

512 Hodges, J.T.: Automated high-resolution frequency-stabilized cavity ring-down absorption spectrometer. *Rev. Sci.*  
513 *Instrum.* 76, 023112. <https://doi.org/10.1063/1.1850633>, 2005.

514 Hodges, J.T., Layer, H.P., Miller, W., Scace, G.E.: Frequency-stabilized single-mode cavity ring-down apparatus  
515 for high-resolution absorption spectroscopy. *Rev. Sci. Instrum.* 75, 849–863.  
516 <https://doi.org/10.1063/1.1666984>, 2004.

517 Keppel-Aleks, G., Toon, G.C., Wennberg, P.O., Deutscher, N.M.: Reducing the impact of source brightness  
518 fluctuations on spectra obtained by Fourier-transform spectrometry. *Appl. Opt.* 46, 4774.  
519 <https://doi.org/10.1364/AO.46.004774>, 2007.

520 Lamouroux, J., Sironneau, V., Hodges, J.T., Hartmann, J.-M.: Isolated line shapes of molecular oxygen:  
521 Requantized classical molecular dynamics calculations versus measurements. *Phys. Rev. A* 89, 042504.  
522 <https://doi.org/10.1103/PhysRevA.89.042504>, 2014.

523 Leshchishina, O., Kassı, S., Gordon, I.E., Rothman, L.S., Wang, L., Campargue, A.: High sensitivity CRDS of the  
524 a<sup>1</sup>Δ<sub>g</sub>←X<sup>3</sup>Σ<sub>g</sub><sup>-</sup> band of oxygen near 1.27 μm: Extended observations, quadrupole transitions, hot bands and  
525 minor isotopologues. *J. Quant. Spectrosc. Radiat. Transf.*, XVIth Symposium on High Resolution  
526 Molecular Spectroscopy (HighRus-2009) XVIth Symposium on High Resolution Molecular Spectroscopy  
527 111, 2236–2245. <https://doi.org/10.1016/j.jqsrt.2010.05.014>, 2010.

528 Leshchishina, O., Kassı, S., Gordon, I.E., Yu, S., Campargue, A.: The band of <sup>16</sup>O<sup>17</sup>O, <sup>17</sup>O<sup>18</sup>O and <sup>17</sup>O<sub>2</sub> by high  
529 sensitivity CRDS near 1.27 μm. *J. Quant. Spectrosc. Radiat. Transf.* 112, 1257–1265.  
530 <https://doi.org/10.1016/j.jqsrt.2011.01.014>, 2011.

531 Lévy, A., Lacombe, N., Chackerian Jr., C.: Collisional Line Mixing A2 - Weber, K. Narahari Rao Alfons, in:  
532 Spectroscopy of the Earth's Atmosphere and Interstellar Medium. Academic Press, pp. 261–337, 1992.

533 Lin, H., Reed, Z.D., Sironneau, V.T., Hodges, J.T.: Cavity ring-down spectrometer for high-fidelity molecular  
534 absorption measurements. *J. Quant. Spectrosc. Radiat. Transf.* 161, 11–20.  
535 <https://doi.org/10.1016/j.jqsrt.2015.03.026>, 2015.

536 Lin, J.C., Gerbig, C., Wofsy, S.C., Daube, B.C., Matross, D.M., Chow, V.Y., Gottlieb, E., Andrews, A.E.,  
537 Pathmathevan, M., Munger, J.W.: What have we learned from intensive atmospheric sampling field  
538 programmes of CO<sub>2</sub>? *Tellus B* 58, 331–343. <https://doi.org/10.1111/j.1600-0889.2006.00202.x>, 2006.

539 Long, D.A., Havey, D.K., Okumura, M., Miller, C.E., Hodges, J.T.: O<sub>2</sub> A-band line parameters to support  
540 atmospheric remote sensing. *J. Quant. Spectrosc. Radiat. Transf.* 111, 2021–2036.  
541 <https://doi.org/10.1016/j.jqsrt.2010.05.011>, 2010.

542 Maté, B., Lugez, C., Fraser, G.T., Lafferty, W.J.: Absolute intensities for the O<sub>2</sub> 1.27 μm continuum absorption. *J.*  
543 *Geophys. Res. Atmospheres* 104, 30585–30590. <https://doi.org/10.1029/1999JD900824>, 1999.

544 Mendonca, J., Strong, K., Toon, G.C., Wunch, D., Sung, K., Deutscher, N.M., Griffith, D.W.T., Franklin, J.E.:  
545 Improving atmospheric CO<sub>2</sub> retrievals using line mixing and speed-dependence when fitting high-  
546 resolution ground-based solar spectra. *J. Mol. Spectrosc., Atmospheric Spectroscopy* 323, 15–27.  
547 <https://doi.org/10.1016/j.jms.2016.01.007>, 2016.

548 Mertz, L.: Auxiliary computation for Fourier spectrometry. *Infrared Phys.* 7, 17–23. [https://doi.org/10.1016/0020-0891\(67\)90026-7](https://doi.org/10.1016/0020-0891(67)90026-7), 1967.

550 Messerschmidt, J., Macatangay, R., Notholt, J., Petri, C., Warneke, T., Weinzierl, C.: Side by side measurements of  
551 CO<sub>2</sub> by ground-based Fourier transform spectrometry (FTS): SIDE BY SIDE MEASUREMENTS OF CO<sub>2</sub>  
552 BY FTS. *Tellus B* 62, 749–758. <https://doi.org/10.1111/j.1600-0889.2010.00491.x>, 2010.

553 Mlawer, E.J., Clough, S.A., Brown, P.D., Stephen, T.M., Landry, J.C., Goldman, A., Murcray, F.J.: Observed  
554 atmospheric collision-induced absorption in near-infrared oxygen bands. *J. Geophys. Res. Atmospheres*  
555 103, 3859–3863. <https://doi.org/10.1029/97JD03141>, 1998.

556 Newman, S.M., Lane, I.C., Orr-Ewing, A.J., Newnham, D.A., Ballard, J.: Integrated absorption intensity and  
557 Einstein coefficients for the O<sub>2</sub> a<sup>1</sup>Δ<sub>g</sub>-X<sup>3</sup>Σ<sub>g</sub><sup>-</sup> (0,0) transition: A comparison of cavity ringdown and high  
558 resolution Fourier transform spectroscopy with a long-path absorption cell. *J. Chem. Phys.* 110, 10749–  
559 10757. <https://doi.org/10.1063/1.479018>, 1999.

560 Newman, S.M., Orr-Ewing, A.J., Newnham, D.A., Ballard, J.: Temperature and pressure dependence of line widths  
561 and integrated absorption intensities for the O<sub>2</sub> a<sup>1</sup>Δ<sub>g</sub> - X<sup>3</sup>Σ<sub>g</sub><sup>-</sup> (0,0) transition. *J. Phys. Chem. A* 104, 9467–  
562 9480, 2000.

563 Ngo, N.H., Lisak, D., Tran, H., Hartmann, J.-M.: An isolated line-shape model to go beyond the Voigt profile in  
564 spectroscopic databases and radiative transfer codes. *J. Quant. Spectrosc. Radiat. Transf.* 129, 89–100.  
565 <https://doi.org/10.1016/j.jqsrt.2013.05.034>, 2013.

566 Predoi-Cross, A., Hambrook, K., Keller, R., Povey, C., Schofield, I., Hurtmans, D., Over, H., Mellau, G.C.:  
567 Spectroscopic lineshape study of the self-perturbed oxygen A-band. *J. Mol. Spectrosc.* 248, 85–110.  
568 <https://doi.org/10.1016/j.jms.2007.11.007>, 2008.

569 Rohart, F., Mäder, H., Nicolaisen, H.-W.: Speed dependence of rotational relaxation induced by foreign gas  
570 collisions: Studies on CH<sub>3</sub>F by millimeter wave coherent transients. *J. Chem. Phys.* 101, 6475–6486.  
571 <https://doi.org/10.1063/1.468342>, 1994.

572 Rothman, L.S., Gordon, I.E., Babikov, Y., Barbe, A., Chris Benner, D., Bernath, P.F., Birk, M., Bizzocchi, L.,  
573 Boudon, V., Brown, L.R., Campargue, A., Chance, K., Cohen, E.A., Coudert, L.H., Devi, V.M., Drouin,  
574 B.J., Fayt, A., Flaud, J.-M., Gamache, R.R., Harrison, J.J., Hartmann, J.-M., Hill, C., Hodges, J.T.,  
575 Jacquemart, D., Jolly, A., Lamouroux, J., Le Roy, R.J., Li, G., Long, D.A., Lyulin, O.M., Mackie, C.J.,  
576 Massie, S.T., Mikhailenko, S., Müller, H.S.P., Naumenko, O.V., Nikitin, A.V., Orphal, J., Perevalov, V.,  
577 Perrin, A., Polovtseva, E.R., Richard, C., Smith, M.A.H., Starikova, E., Sung, K., Tashkun, S., Tennyson,  
578 J., Toon, G.C., Tyuterev, V.G., Wagner, G.: The HITRAN2012 molecular spectroscopic database. *J. Quant.*  
579 *Spectrosc. Radiat. Transf., HITRAN2012 special issue* 130, 4–50.  
580 <https://doi.org/10.1016/j.jqsrt.2013.07.002>, 2013.

581 Rothman, L.S., Gordon, I.E., Barbe, A., Benner, D.C., Bernath, P.F., Birk, M., Boudon, V., Brown, L.R.,  
582 Campargue, A., Champion, J.-P., Chance, K., Coudert, L.H., Dana, V., Devi, V.M., Fally, S., Flaud, J.-M.,  
583 Gamache, R.R., Goldman, A., Jacquemart, D., Kleiner, I., Lacombe, N., Lafferty, W.J., Mandin, J.-Y.,  
584 Massie, S.T., Mikhailenko, S.N., Miller, C.E., Moazzen-Ahmadi, N., Naumenko, O.V., Nikitin, A.V.,  
585 Orphal, J., Perevalov, V.I., Perrin, A., Predoi-Cross, A., Rinsland, C.P., Rotger, M., Šimečková, M., Smith,  
586 M.A.H., Sung, K., Tashkun, S.A., Tennyson, J., Toth, R.A., Vandaele, A.C., Vander Auwera, J.: The  
587 HITRAN 2008 molecular spectroscopic database. *J. Quant. Spectrosc. Radiat. Transf., HITRAN* 110, 533–  
588 572. <https://doi.org/10.1016/j.jqsrt.2009.02.013>, 2009.

589 Rothman, L.S., Jacquemart, D., Barbe, A., Chris Benner, D., Birk, M., Brown, L.R., Carleer, M.R., Chackerian Jr.,  
590 C., Chance, K., Coudert, L.H., Dana, V., Devi, V.M., Flaud, J.-M., Gamache, R.R., Goldman, A.,  
591 Hartmann, J.-M., Jucks, K.W., Maki, A.G., Mandin, J.-Y., Massie, S.T., Orphal, J., Perrin, A., Rinsland,  
592 C.P., Smith, M.A.H., Tennyson, J., Tolchenov, R.N., Toth, R.A., Vander Auwera, J., Varanasi, P., Wagner,  
593 G.: The HITRAN 2004 molecular spectroscopic database. *J. Quant. Spectrosc. Radiat. Transf.* 96, 139–204.  
594 <https://doi.org/10.1016/j.jqsrt.2004.10.008>, 2005.

595 Shannon, I., Harris, M., McHugh, D.R., Lewis, E.L.: Low-pressure spectral line profiles: an analysis in terms of  
596 symmetric speed-dependent Voigt profiles. *J. Phys. B At. Mol. Phys.* 19, 1409.  
597 <https://doi.org/10.1088/0022-3700/19/10/011>, 1986.

598 Singh, H.B., Brune, W.H., Crawford, J.H., Jacob, D.J., Russell, P.B.: Overview of the summer 2004 Intercontinental  
599 Chemical Transport Experiment-North America (INTEX-A). *J. Geophys. Res. Atmospheres* 111, D24S01.  
600 <https://doi.org/10.1029/2006JD007905>, 2006.

601 Smith, K.M., Newnham, D.A.: Near-infrared absorption cross sections and integrated absorption intensities of  
602 molecular oxygen (O<sub>2</sub>, O<sub>2</sub>-O<sub>2</sub>, and O<sub>2</sub>-N<sub>2</sub>). *J. Geophys. Res. Atmospheres* 105, 7383–7396.  
603 <https://doi.org/10.1029/1999JD901171>, 2000.

604 Smith, K.M., Newnham, D.A., Williams, R.G.: Collision-induced absorption of solar radiation in the atmosphere by  
605 molecular oxygen at 1.27 μm: Field observations and model calculations. *J. Geophys. Res. Atmospheres*  
606 106, 7541–7552. <https://doi.org/10.1029/2000JD900699>, 2001.

607 Strong, K., Mendonca, J., Weaver, D., Fogal, P., Drummond, J.R., Batchelor, R., Lindenmaier, R.: TCCON data  
608 from Eureka (CA), Release GGG2014.R1. <https://doi.org/10.14291/tcon.ggg2014.eureka01.R1/1325515>,  
609 2017.

610 Toon, G. C.: Telluric line list for GGG2014, TCCON data archive. Carbon Dioxide Inf. Anal. Cent. Oak Ridge Natl.  
611 Lab. Oak Ridge Tenn. USA. <https://doi.org/10.14291/tcon.ggg2014.atm.R0/1221656>, 2014a.

612 Toon, G. C.: Solar line list for GGG2014. TCCON Data Arch. Hosted Carbon Dioxide Inf. Anal. Cent. Oak Ridge  
613 Natl. Lab. Oak Ridge Tenn. USA, 2014b.

614 Toon, G.C.: The JPL MkIV interferometer. *Opt. Photonics News* 2, 19–21.  
615 <https://doi.org/10.1364/OPN.2.10.000019>, 1991.

616 Tran, H., Boulet, C., Hartmann, J.-M.: Line mixing and collision-induced absorption by oxygen in the A band:  
617 Laboratory measurements, model, and tools for atmospheric spectra computations. *J. Geophys. Res.*  
618 *Atmospheres* 111, D15210. <https://doi.org/10.1029/2005JD006869>, 2006.

619 Tran, H., Hartmann, J.-M.: An improved O<sub>2</sub> A band absorption model and its consequences for retrievals of photon  
620 paths and surface pressures. *J. Geophys. Res. Atmospheres* 113, D18104.  
621 <https://doi.org/10.1029/2008JD010011>, 2008.

622 Tran, H., Ngo, N.H., Hartmann, J.-M.: Efficient computation of some speed-dependent isolated line profiles. *J.*  
623 *Quant. Spectrosc. Radiat. Transf.* 129, 199–203. <https://doi.org/10.1016/j.jqsrt.2013.06.015>, 2013.

624 Wallace, L., Livingston, W.: Spectroscopic observations of atmospheric trace gases over Kitt Peak. I - Carbon  
625 dioxide and methane from 1979 to 1985. *J. Geophys. Res.* 95, 9823–9827.  
626 <https://doi.org/10.1029/JD095iD07p09823>, 1990.

627 Washenfelder, R.A., Toon, G.C., Blavier, J.-F., Yang, Z., Allen, N.T., Wennberg, P.O., Vay, S.A., Matross, D.M.,  
628 Daube, B.C.: Carbon dioxide column abundances at the Wisconsin Tall Tower site. *J. Geophys. Res.*  
629 *Atmospheres* 111, D22305. <https://doi.org/10.1029/2006JD007154>, 2006.

630 Wehr, R.A.: Dicke -narrowed spectral lines in carbon monoxide buffered by argon (Ph.D.). University of Toronto  
631 (Canada), Canada, 2005.

632 Wennberg, P.O., Roehl, C.M., Wunch, D., Toon, G.C., Blavier, J.-F., Washenfelder, R., Keppel-Aleks, G., Allen,  
633 N.T., Ayers, J.: TCCON data from Park Falls (US), Release GGG2014.R0.  
634 <https://doi.org/10.14291/tcon.ggg2014.parkfalls01.R0/1149161>, 2017a.

635 Wennberg, P.O., Wunch, D., Roehl, C.M., Blavier, J.-F., Toon, G.C., Allen, N.T., Dowell, P., Teske, K., Martin, C.,  
636 Martin, J.: TCCON data from Lamont (US), Release GGG2014.R0.  
637 <https://doi.org/10.14291/tcon.ggg2014.lamont01.R0/1149159>, 2017b.

638 Wofsy, S.C.: HIAPER Pole-to-Pole Observations (HIPPO): fine-grained, global-scale measurements of climatically  
639 important atmospheric gases and aerosols. *Philos. Trans. R. Soc. Lond. Math. Phys. Eng. Sci.* 369, 2073–  
640 2086. <https://doi.org/10.1098/rsta.2010.0313>, 2011.

641 Wójtewicz, S., Cygan, A., Masłowski, P., Domysławska, J., Lisak, D., Trawiński, R.S., Ciuryło, R.: Spectral line  
642 shapes of self-broadened P-branch transitions of oxygen B band. *J. Quant. Spectrosc. Radiat. Transf.* 144,  
643 36–48. <https://doi.org/10.1016/j.jqsrt.2014.03.029>, 2014.

644 Wunch, D., Toon, G.C., Blavier, J.-F.L., Washenfelder, R.A., Notholt, J., Connor, B.J., Griffith, D.W.T., Sherlock,  
645 V., Wennberg, P.O.: The Total Carbon Column Observing Network. *Philos. Trans. R. Soc. Math. Phys.*  
646 *Eng. Sci.* 369, 2087–2112. <https://doi.org/10.1098/rsta.2010.0240>, 2011.

647 Wunch, D., Toon, G.C., Sherlock, V., Deutscher, N.M., Liu, C., Feist, D.G., Wennberg, P.O.: The Total Carbon  
648 Column Observing Network’s GGG2014 Data Version.  
649 <https://doi.org/10.14291/tcon.ggg2014.documentation.R0/1221662>, 2015.

650 Wunch, D., Toon, G.C., Wennberg, P.O., Wofsy, S.C., Stephens, B.B., Fischer, M.L., Uchino, O., Abshire, J.B.,  
651 Bernath, P., Biraud, S.C., Blavier, J.-F.L., Boone, C., Bowman, K.P., Browell, E.V., Campos, T., Connor,  
652 B.J., Daube, B.C., Deutscher, N.M., Diao, M., Elkins, J.W., Gerbig, C., Gottlieb, E., Griffith, D.W.T.,  
653 Hurst, D.F., Jiménez, R., Keppel-Aleks, G., Kort, E.A., Macatangay, R., Machida, T., Matsueda, H.,

654 Moore, F., Morino, I., Park, S., Robinson, J., Roehl, C.M., Sawa, Y., Sherlock, V., Sweeney, C., Tanaka,  
655 T., Zondlo, M.A.: Calibration of the Total Carbon Column Observing Network using aircraft profile data.  
656 Atmos Meas Tech 3, 1351–1362. <https://doi.org/10.5194/amt-3-1351-2010>, 2010.

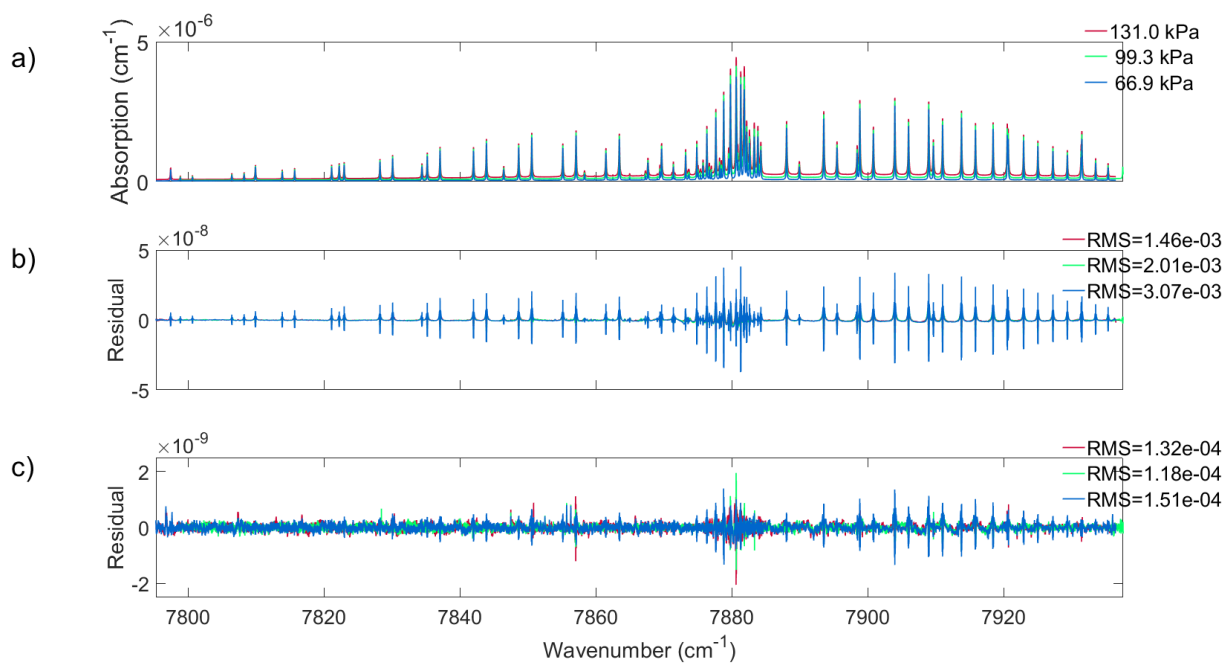
657 Yang, Z., Toon, G.C., Margolis, J.S., Wennberg, P.O.: Atmospheric CO<sub>2</sub> retrieved from ground-based near IR solar  
658 spectra. Geophys. Res. Lett. 29, 1339. <https://doi.org/10.1029/2001GL014537>, 2002.

659 Yokota, T., Yoshida, Y., Eguchi, N., Ota, Y., Tanaka, T., Watanabe, H., Maksyutov, S.: Global Concentrations of  
660 CO<sub>2</sub> and CH<sub>4</sub> Retrieved from GOSAT: First Preliminary Results. Sola 5, 160–163.  
661 <https://doi.org/10.2151/sola.2009-041>, 2009.

662 Yu, S., Drouin, B.J., Miller, C.E.: High resolution spectral analysis of oxygen. IV. Energy levels, partition sums,  
663 band constants, RKR potentials, Franck-Condon factors involving the X<sup>3</sup>Σ<sub>g</sub><sup>-</sup>, a<sup>1</sup>Δ<sub>g</sub> and b<sup>1</sup>Σ<sub>g</sub><sup>+</sup> states. J.  
664 Chem. Phys. 141, 174302. <https://doi.org/10.1063/1.4900510>, 2014.

665  
666  
667  
668  
669  
670  
671  
672  
673  
674  
675  
676  
677  
678  
679  
680  
681  
682  
683  
684  
685  
686  
687  
688  
689

690 **Figures**



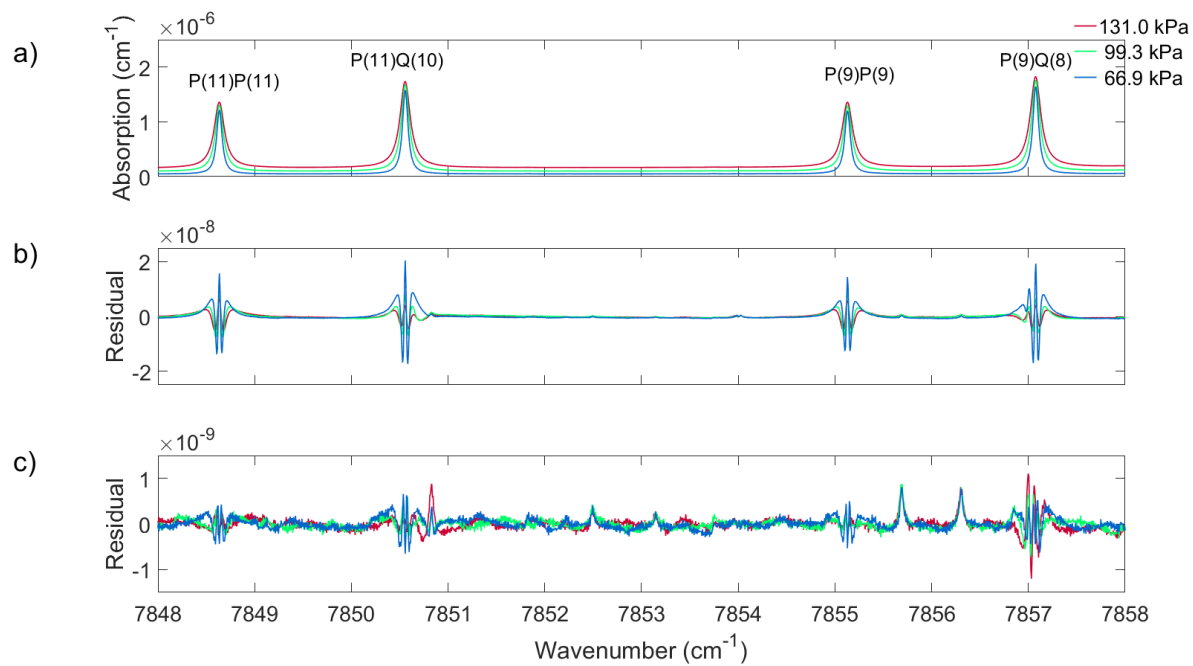
691

692 **Figure 1: (a) Cavity-ring-down absorption coefficients for  $\text{O}_2$  measured at the three pressures indicated in the**  
693 **legend at approximately room temperature and a volume mixing ratio of 0.20720(43). The difference between**  
694 **measured absorption coefficients and those calculated using (b) a Voigt line shape, and (c) the speed-**  
695 **dependent Voigt line shape. Note the difference in scale between panels (b) and (c).**

696

697

698



699

700 **Figure 2: The same as Figure 1 but expanded to show four spectral lines in the P branch of the O<sub>2</sub> 1.27 μm**  
 701 **band.**

702

703

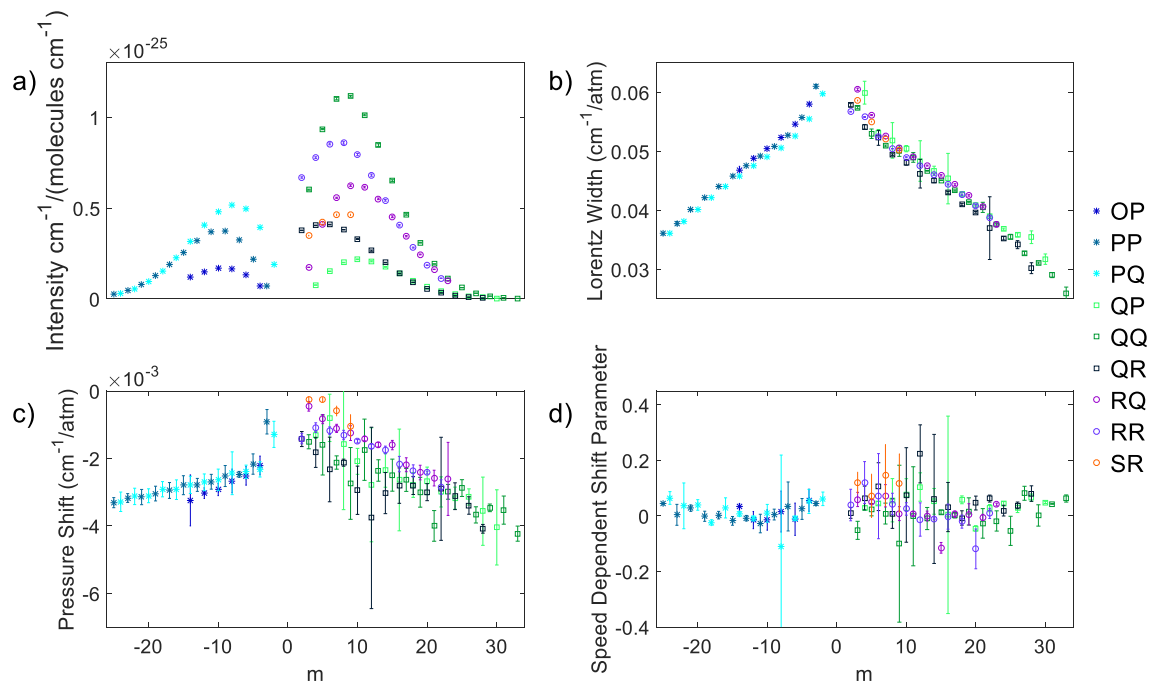
704

705

706

707

708



709

710 **Figure 3: The averaged measured (a) intensity, (b) Lorentz line width, (c) pressure shift, and (d) speed-**  
 711 **dependent pressure shift retrieved from the three cavity ring-down spectra of the 1.27  $\mu\text{m}$  band of  $\text{O}_2$ . All**  
 712 **data are plotted as a function of  $m$  which is  $m=-J$  for the P-branch lines,  $m=J$  for the Q-branch, and  $m=J+1$**   
 713 **for the R-branch (where  $J$  is the lower state rotational quantum number) and the uncertainties shown are  $2\sigma$ .**

714

715

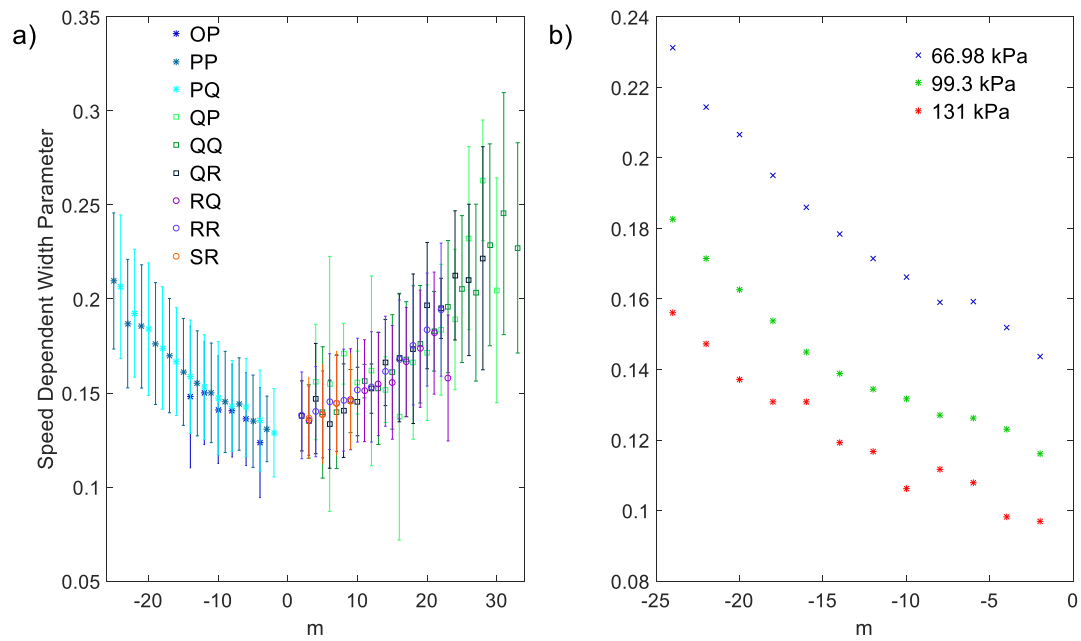
716

717

718

719

720



721

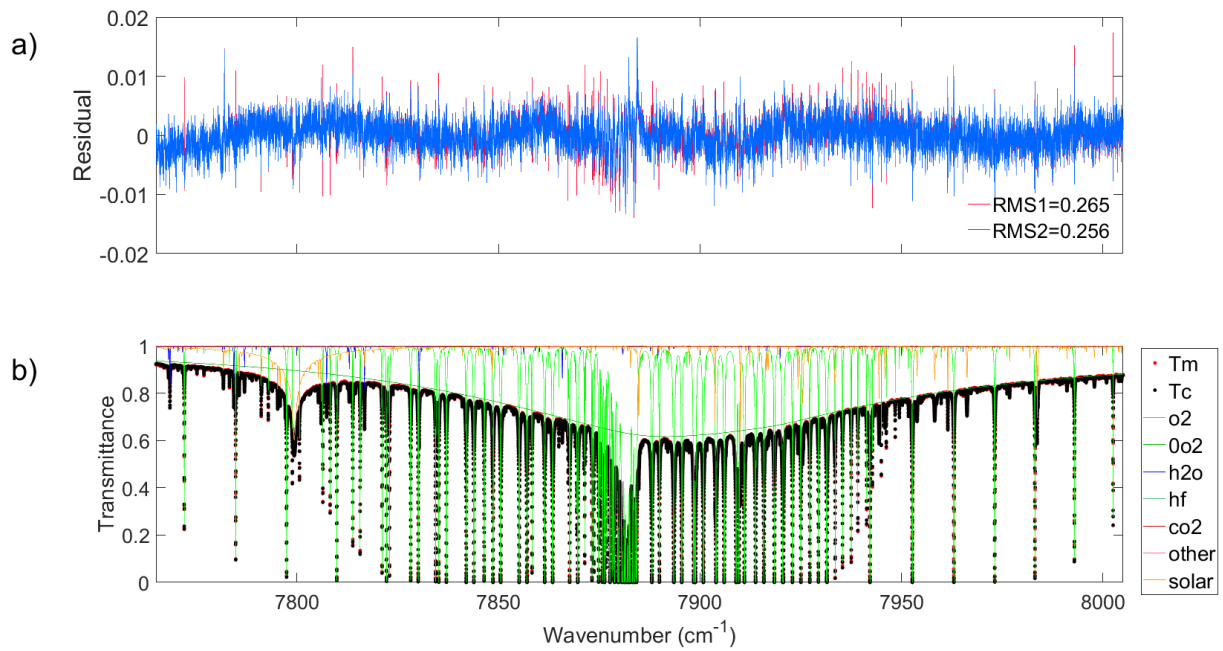
722 **Figure 4: (a) The averaged measured speed-dependent width parameter of the 1.27  $\mu\text{m}$  band of  $\text{O}_2$  plotted as**  
 723 **a function of m. (b) The measured speed-dependent width parameter for spectral lines that belong to the PQ**  
 724 **sub-branch plotted as a function of m.**

725

726

727

728



729

730 **Figure 5: (a) The residuals (measured minus calculated) for a spectrum measured at Eureka on March 27,**  
 731 **2015 at a SZA of 81.32°. The red residual is the result of using the Voigt line shape and the blue is from using**  
 732 **the qSDV. (b) The measured (red dots) and calculated (black dots), with the qSDV, spectrum, along with the**  
 733 **gases included in the fit (refer to the legend to the right) in the spectral window.**

734

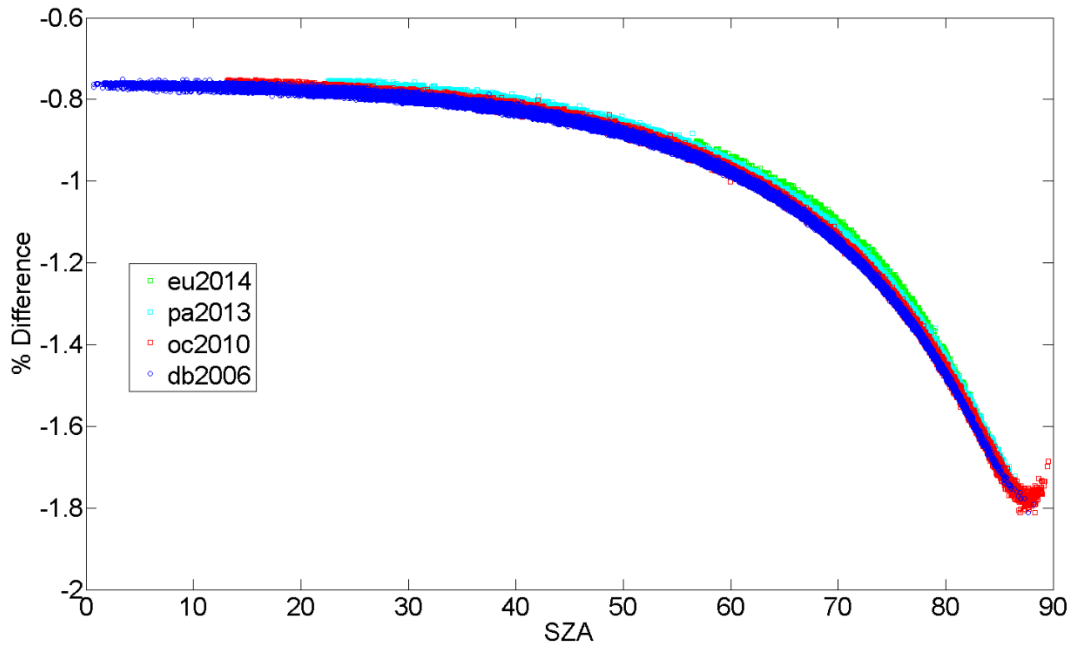
735

736

737

738

739



740

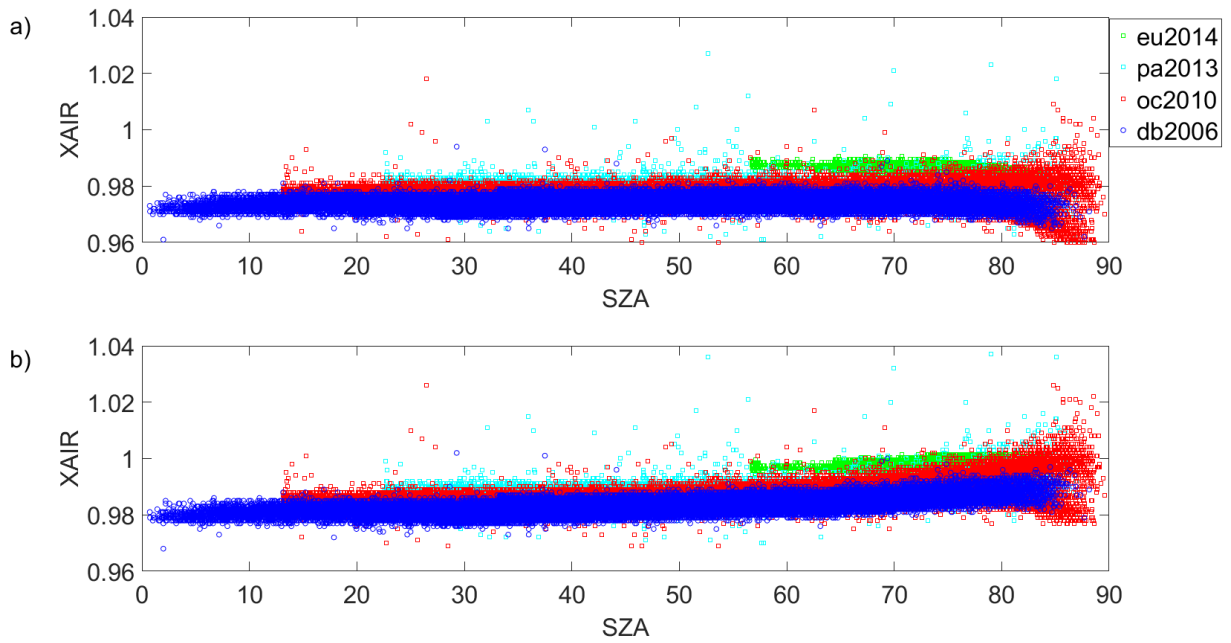
741 **Figure 6: The percent difference between the O<sub>2</sub> column retrieved with the Voigt and qSDV line shapes for a**  
 742 **year of measurements from Eureka (eu), Park Falls (pa), Lamont (oc), and Darwin (db).**

743

744

745

746



747

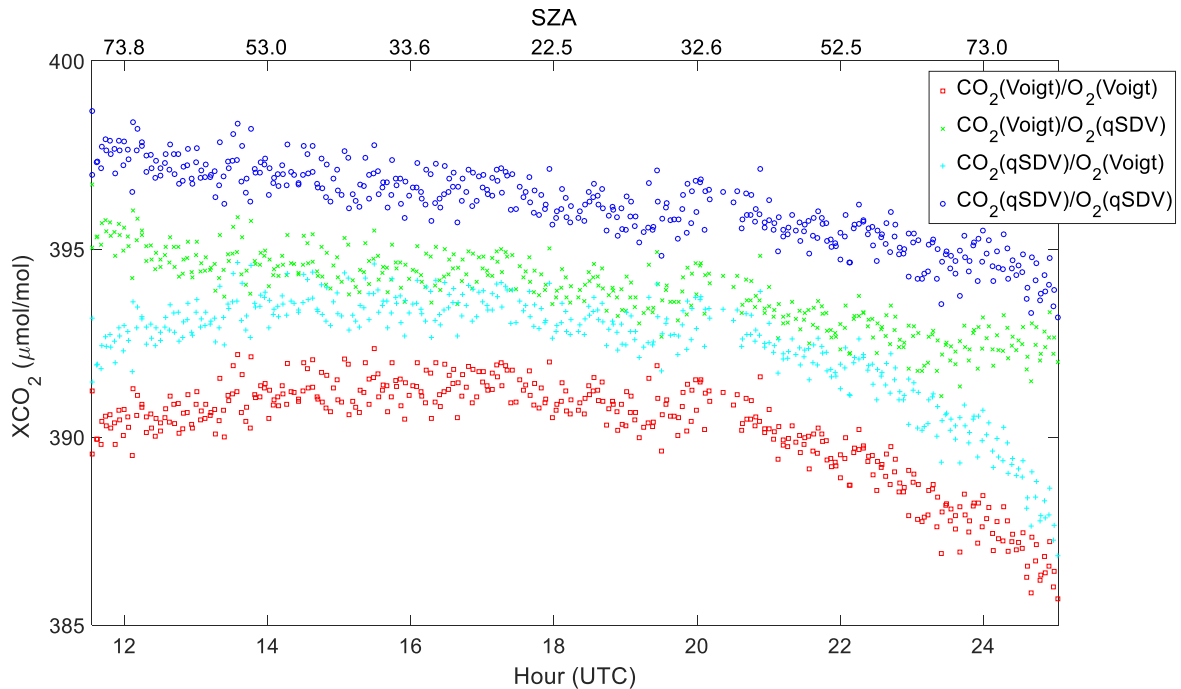
748 **Figure 7: XAIR from Park Falls retrieved from spectra recorded on June 18, 2013. XAIR is calculated using**  
 749 **O<sub>2</sub> columns retrieved using a Voigt (red) and qSDV (green) line shapes. The top x-axis is the SZA that**  
 750 **corresponds to the hour on the bottom x-axis. (a) XAIR as a function of SZA calculated using the total**  
 751 **column of O<sub>2</sub> retrieved using the Voigt line shape. (b) is the same as (a) except the total column of O<sub>2</sub> was**  
 752 **retrieved with the qSDV.**

753

754

755

756

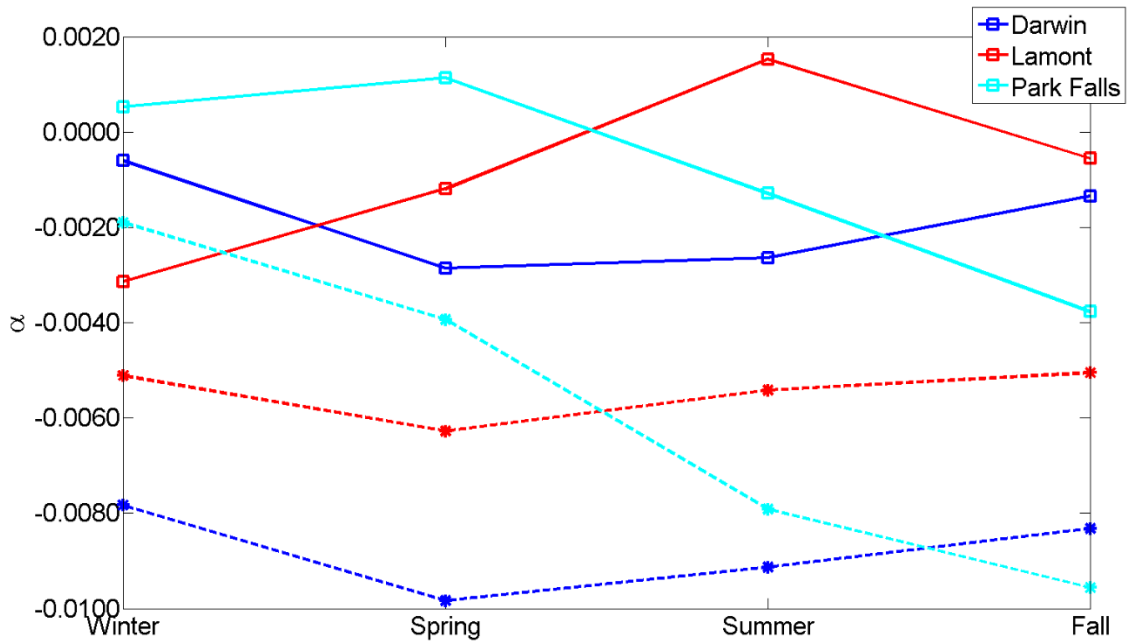


757

758 **Figure 8: XCO<sub>2</sub> calculated from the CO<sub>2</sub> and O<sub>2</sub> columns retrieved from Park Falls spectra recorded on June**  
 759 **18, 2013. The CO<sub>2</sub> columns were retrieved using either the Voigt line shape or the qSDV with line mixing,**  
 760 **while the O<sub>2</sub> columns were retrieved using either the Voigt or qSDV line shapes. XCO<sub>2</sub> was calculated in**  
 761 **four ways: 1) Both CO<sub>2</sub> and O<sub>2</sub> columns retrieved using the Voigt line shape (red), 2) CO<sub>2</sub> columns retrieved**  
 762 **with the Voigt and O<sub>2</sub> columns retrieved with the qSDV (green), 3) CO<sub>2</sub> columns retrieved with the qSDV**  
 763 **and line mixing and O<sub>2</sub> columns retrieved with the Voigt (cyan), and 4) CO<sub>2</sub> columns retrieved with the qSDV**  
 764 **and line mixing and O<sub>2</sub> columns retrieved with the qSDV (blue). The top x-axis is the SZA that corresponds**  
 765 **to the hour on the bottom x-axis.**

766

767



768

769 **Figure 9:** The average air mass-dependent correction factor for XCO<sub>2</sub> derived from a year of spectra  
 770 measured at Darwin, Lamont, and Park Falls for different seasons. The dashed lines with stars are the  $\alpha$  for  
 771 XCO<sub>2</sub> retrieved using a Voigt line shape for both CO<sub>2</sub> and O<sub>2</sub> columns. The solid lines with squares are from  
 772 XCO<sub>2</sub> retrieved using the qSDV for both CO<sub>2</sub> and O<sub>2</sub> columns.

773

774

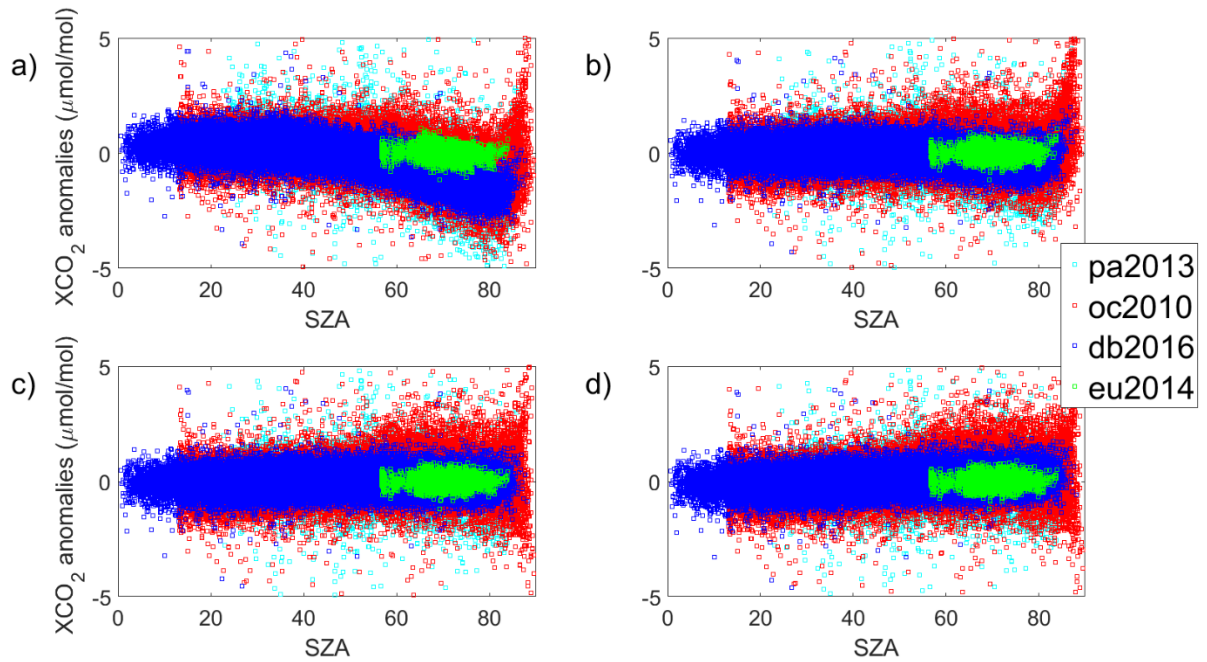
775

776

777

778

779



780

781 **Figure 10: (a) XCO<sub>2</sub> Voigt anomaly for a year of measurements from the four TCCON sites. The XCO<sub>2</sub>**  
 782 **anomaly is the difference between each XCO<sub>2</sub> value and the daily median XCO<sub>2</sub>. (b) The XCO<sub>2</sub> Voigt**  
 783 **anomaly after the airmass dependence correction is applied to the XCO<sub>2</sub> Voigt data. (c) XCO<sub>2</sub> qSDV**  
 784 **anomaly. (d) XCO<sub>2</sub> qSDV anomaly after correction for the airmass dependence.**

785

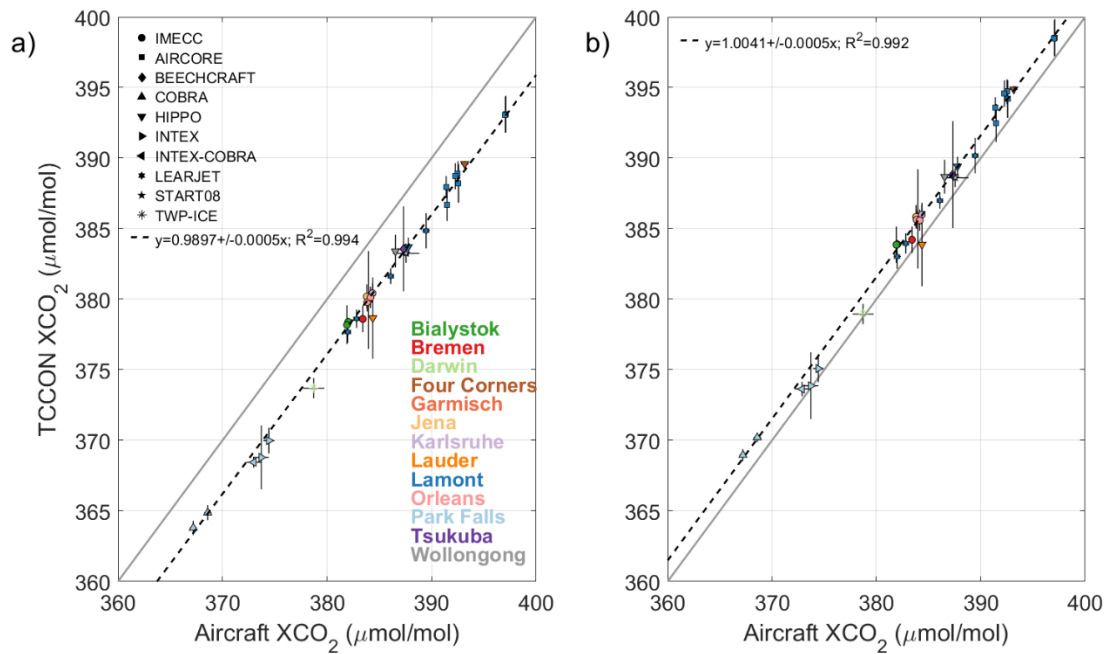
786

787

788

789

790



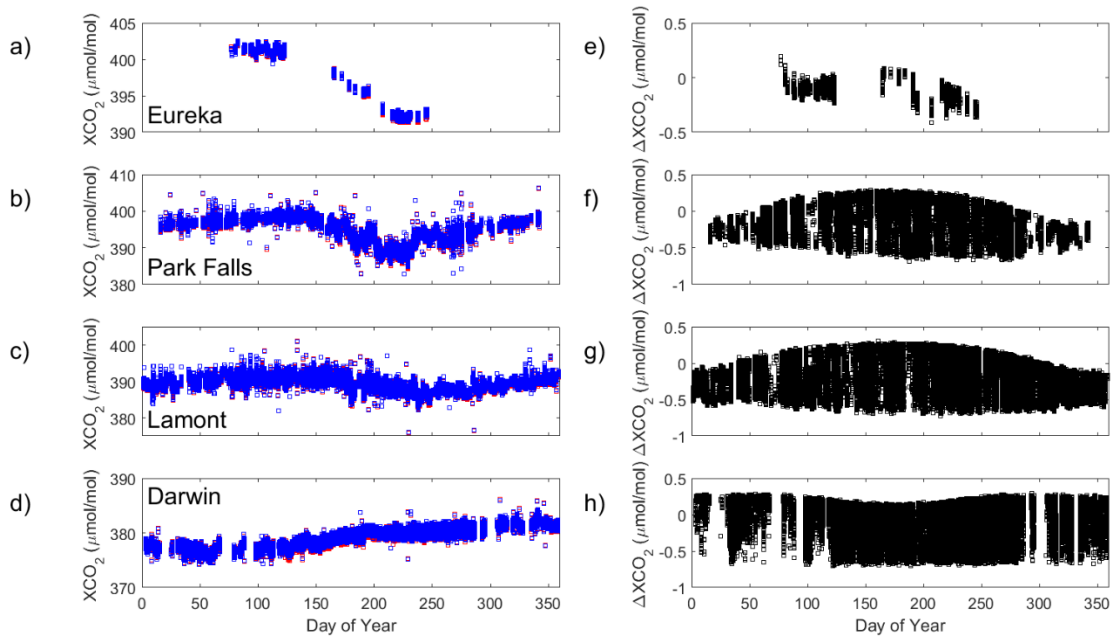
791

792 **Figure 11: (a) Correlation between TCCON and aircraft XCO<sub>2</sub> Voigt measurements for 13 TCCON sites.**  
 793 **Each aircraft type is indicated by a different symbol given by the legend in the top left corner. Each site is**  
 794 **represented by a different colour given by the legend in the bottom right corner. The grey line indicates the**  
 795 **one-to-one line and the dashed line is the line of best fit for the data. The slope of the line of best fit as well as**  
 796 **the error on the slope are given in the plot. (b) the same as (a) but for XCO<sub>2</sub> qSDV.**

797

798

799



800

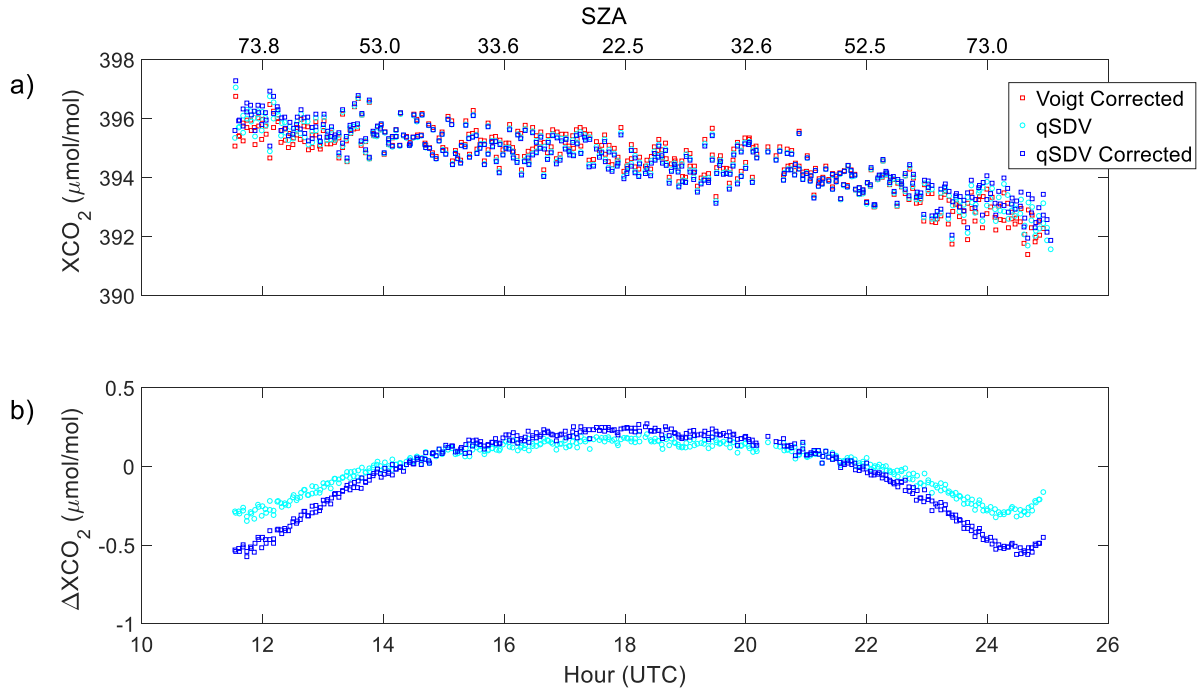
801 **Figure 12: (a) to (d) XCO<sub>2</sub> plotted as a function of day of the year for Eureka (2014), Park Falls (2013),**  
 802 **Lamont (2010), and Darwin (2006) respectively. The mostly-hidden red boxes are XCO<sub>2</sub> calculated from**  
 803 **using a Voigt line shape in the retrieval and the blue boxes are from using the qSDV. (e) to (h) the difference**  
 804 **between XCO<sub>2</sub> Voigt and XCO<sub>2</sub> qSDV.**

805

806

807

808



809

810 **Figure 13: (a) XCO<sub>2</sub> from Park Falls retrieved from spectra recorded on June 18, 2013. Plotted is XCO<sub>2</sub>**  
811 **retrieved: (1) with a Voigt line shape and corrected for the airmass dependence (red squares), (2) with the**  
812 **qSDV (cyan circles), and (3) with the qSDV and corrected for the airmass dependence (blue squares). (b) the**  
813 **difference between the Voigt XCO<sub>2</sub> corrected and the qSDV XCO<sub>2</sub> (cyan circles), and the difference between**  
814 **the Voigt XCO<sub>2</sub> corrected and the qSDV XCO<sub>2</sub> corrected (blue squares). The top x-axis is the SZA that**  
815 **corresponds to the hour on the bottom x-axis.**

816